



Subseasonal variability of sea level pressure and its influence on snowpack over mid-high-latitude Eurasia during boreal winter

Yalu Ru¹ · Xuejuan Ren¹

Received: 16 November 2023 / Accepted: 8 July 2024 / Published online: 30 July 2024
© The Author(s) 2024

Abstract

The atmospheric circulation significantly influences the snowpack over mid-high-latitude Eurasia. This study examines the characteristics of the leading subseasonal variability mode of boreal winter sea level pressure (SLP) with 20–80-day period and its relationship with snowpack over mid-high-latitude Eurasia, using the fifth generation of European Center for Medium-Range Weather Forecasts (ECMWF) reanalysis (ERA5) data and different snowpack datasets. The SLP leading mode, characterized by a monopole pattern with a strong surface anomalous high centered near the Ural Mountains, exhibits a barotropic structure and extends from the surface to the tropopause. Above SLP and geopotential height anomalies propagate southeastward from the Barents-Kara Sea to East Asia. This leading SLP mode contributes to surface air temperature (SAT) and snowfall circulation anomalies over mid-high-latitude Eurasia. The latter two both directly influence on snowpack anomalies in situ. Over high latitude region, snowfall circulation anomaly is the dominant factor to control the snow depth anomaly. Over middle latitude region, both SAT and snowfall circulation anomalies lead to the snowpack anomaly. Furthermore, the response of snow depth to the leading subseasonal SLP mode occurs 2–5 days earlier than the response of snow cover to the same mode over middle latitude region. In addition, it is suggested that the Arctic Oscillation (AO), East Atlantic/West Russia (EAWR) and Polar/Eurasia (PEU) pattern may contribute to the development of the leading SLP mode and subsequently influence snowpack anomalies.

Keywords Sea level pressure · Boreal winter subseasonal variability · Snow depth and snow cover · Surface air temperature · Snowfall circulation · Atmospheric teleconnections over mid-high latitudes

1 Introduction

In the literature, numerous studies have focused on subseasonal variability, with time ranging from 10 days to 90 days. In the tropics, it mainly features a periodicity of 30–60 days and eastward (northward) propagation during boreal winter (summer), namely MJO (BSISO) (Madden and Julian 1971; Sperber 2003; Wheeler and Hendon 2004; Lee et al. 2013; Wang et al. 2018). MJO and BSISO are directly triggered by convection, accompanying with baroclinic structure (Jiang et al. 2004; Yang and Ingersoll 2013; DeMott et al. 2019). Additionally, the subseasonal variability of atmospheric

circulation and snowpack are also observed in mid-high latitudes (Zhu and Yang 2021; Qian et al. 2022; Zhu et al. 2023), particularly during winter (Ding and Krishnamurti 1987; Linkin and Nigam 2008; Lin 2015; Barrett et al. 2015; Li et al. 2016; Yang et al. 2019). These subseasonal variabilities over mid-high-latitude can impact both local and global weather and climate, such as cold surges (Ding 1990; Li et al. 2017), precipitation (Yao et al. 2015; Guan et al. 2020), and extreme warm (cold) events (Xiang et al. 2020; Guan et al. 2020; Ma and Zhu 2023). Thus, it is of great significance to comprehend subseasonal variability over mid-high latitudes (e.g., Li et al. 2017; Xiang et al. 2019; Lin 2020).

The atmospheric circulation over mid-high-latitude Eurasia exhibits robust subseasonal variability during boreal winter (Jiao et al. 2019; Fan et al. 2022; Zhou et al. 2023; Jiang et al. 2023). Many researches have investigated the surface air temperature (SAT) anomalies over this region (Yang and Li 2016; Yao et al. 2016; Xu et al. 2018; Kim

✉ Xuejuan Ren
renxuej@nju.edu.cn

¹ China Meteorological Administration Key Laboratory for Climate Prediction Studies, School of Atmospheric Sciences, Nanjing University, Nanjing 210023, China

et al. 2021; Qin et al. 2022; Zhong and Wu 2022). Previous studies have indicated that SAT anomalies have various periodicities over mid-high-latitude Eurasia, such as 10–60 days (Yang and Li 2016), 10–30 days (Yao et al. 2016; Xiu et al. 2022; Gao et al. 2022), 20–50 days (Xiu et al. 2022; Guan and Wang 2023). Furthermore, the subseasonal SAT variability over mid-high latitude Eurasia exhibits pronounced southeastward propagation from the Arctic to East Asia with equivalent barotropic vertical structure in the troposphere (Yang and Li 2016; Kim et al. 2021; Xiu et al. 2022; Guan and Wang 2023).

Sea level pressure (SLP), as a surface component of atmospheric circulation, has been examined by studies (Trenberth and Paolino 1981; Simonnet and Plaut 2001; Johnson and Feldstein 2010). For example, several studies have investigated the Siberian High (Ding and Krishnamurti 1987; Takaya and Nakamura 2005a, b; Chang and Lu 2012). In terms of time scale, previous studies have mainly concentrated on synoptic time scale or period between 10 and 20 days. In these time scales, the SLP anomaly is featured as a clearly southeastward propagation (e.g. Ding 1990; Takaya and Nakamura 2005a). However, compared with the study about SAT anomaly, the subseasonal SLP anomaly with period between 20 and 80 days over mid-high-latitude Eurasia is lack of investigation in previous studies and needs to be further studied.

Snowpack occupies much of the Northern Hemisphere extratropics from mid-to high latitudes during boreal winter (Luo et al. 2023). The connection between snowpack over the Eurasian continent and the atmospheric circulation on subseasonal time scales is still unclear. Some recent studies addressed that snowpack anomaly can modulate atmospheric circulation anomaly through snow-albedo effect and snow-insulation effect (Gong et al. 2004; Ge and Gong 2010; Li et al. 2018, 2021). On the other hand, it was suggested that the atmospheric circulation can dominate snowpack anomaly (e.g., Guan et al. 2012; Barrett et al. 2015; Li et al. 2016). SAT and snowfall anomalies directly influence snowpack anomaly. Preexisting negative SAT anomalies provide cold conditions for snow accumulation and positive snowpack anomaly. A positive snowfall anomaly leads to a positive snowpack tendency anomaly due to cumulative effects (Song and Wu 2019; Li et al. 2019; You et al. 2020).

Above mentioned three physical processes (snow-albedo effect, snow-insulation effect and atmospheric circulation influence) may have different role over middle and high latitudes of the Eurasian continent (Gong et al. 2004; Zhang 2005; Komatsu et al. 2023). We speculate that, over high latitudes, snow-insulation effect are more dominant than snow-albedo effect because of the solar elevation. Over middle latitudes, the atmospheric circulation may lead snowpack. Thus, atmospheric circulation influence may

be more important over middle latitudes. To prove above points, we diagnose surface energy flux over high latitudes and analyze lead-lag relationship between atmosphere and snowpack over middle latitudes of the Eurasian continent on 20-80-day time scale in this paper. This is distinct from previous studies.

Previous studies have suggested that atmospheric teleconnections over mid-high latitudes can cause atmospheric circulation and surface condition anomalies over the Eurasian continent (Liu et al. 2014; Guan and Wang 2023; Jiang et al. 2023). For instance, the Arctic Oscillation (AO) and North Atlantic Oscillation (NAO) can modulate wave trains, contributing to snow cover (SC) anomaly over middle latitudes (Song and Wu 2019; Song et al. 2019a, b). The Scandinavia (SCAN) pattern can influence snowpack anomaly over Siberia through regulating the strength of Siberian High (Wang and Tan 2020). Based on previous studies, we also investigate the relationship between teleconnections (e.g., AO, NAO, SCAN, the East Atlantic/West Russia pattern and Polar/Eurasia pattern) and SLP over Eurasia on 20-80-day time scale.

This study is to unveil the characteristics of subseasonal SLP variability, with period between 20 and 80 days, and demonstrate the lead-lag relationship between *situ* snowpack and atmospheric circulation factors (surface air temperature and snowfall) over mid-high-latitude Eurasia and related physical processes during boreal winter. We aim to address the following questions: (1) What are the essential features of subseasonal SLP variability over mid-high-latitude Eurasia with period of 20–80 days during boreal winter? (2) What is the evolution of subseasonal snow depth (SD) and snow cover (SC) anomalies associated with the above evolution of SLP anomaly? (3) What are the specific connections and physical processes between the subseasonal SLP and snowpack anomalies over middle and high latitudes of the Eurasian continent? The paper is organized as follows: Sect. 2 describes data and methods. The features of subseasonal SLP variability over mid-high-latitude Eurasia are given in Sect. 3. Section 4 depicts snowpack anomalies associated with the leading subseasonal SLP mode. The physical processes related with the relationship between subseasonal SLP and snowpack anomalies are investigated in Sect. 5. Finally, summary and discussions are provided in Sect. 6.

2 Data and methods

2.1 Atmospheric reanalysis data

We use daily products from the fifth generation of the European Center for Medium-Range Weather Forecasts

(ECMWF) reanalysis (ERA5; Hersbach et al. 2020). The data covers the period from 1 January 1979 to 31 December 2022 with resolution of $1.5^\circ \times 1.5^\circ$. The daily variables include SLP, SAT at 2-meter height, surface winds at 10-meter height, surface energy fluxes (downward shortwave and longwave radiation, net shortwave and longwave radiation, sensible and latent heat fluxes), three-dimensional geopotential height (Z), zonal and meridional winds (u, v), vertical velocity (ω), temperature (T), and specific humidity (q) with 37 vertical levels extending from 1000 to 1 hPa.

2.2 Snowpack data

The daily snowpack datasets used in this study are selected based on two significant criteria: complete Eurasia spatial coverage (with the exception of an alpine mask applied to GlobSnow) and continuous availability throughout the satellite era. The component snowpack datasets analyzed in this study are described below and summarized in Table 1.

Since there is limited knowledge about the subseasonal snow depth variability over Eurasia, four snow depth datasets are selected to reduce uncertainty. The GlobSnow, version 3, snow water equivalent (SWE) dataset combines satellite-based passive microwave radiometer data with ground based synoptic snow depth observations using Bayesian data assimilation, incorporating the HUT Snow Emission model (Luoju et al. 2021). We convert SWE to SD by assuming a constant snow density of 0.24 g cm^{-3} (Luoju et al. 2021). We also use three reanalysis products: version 2 of Modern-Era Retrospective analysis for Research and Applications (MERRA-2; Buchard et al. 2017) by the U.S. National Aeronautics and Space Administration, the Japanese 55-year Reanalysis (JRA-55; Kobayashi et al. 2015) by the Japan Meteorological Agency, and ERA5_Land by ECWMF (Muñoz-Sabater et al. 2021). The representation of snow depth in these reanalysis data differs depending on whether the observed snow data are assimilated or not.

The latest daily snow cover data is the Moderate Resolution Imaging Spectroradiometer (MODIS)/Terra Snow

Cover L3 Global 0.05Deg Climate Modeling Grid (CMG), version 6 (Hall and Riggs 2016) from 24 February 2000 to the present expect for some data outage periods. The quality of the MODIS subseasonal snow cover over Eurasia has been verified by several studies (Xu et al. 2017; Song and Wu 2019; Song et al. 2019a, b). In this study, the original data on a $0.05^\circ \times 0.05^\circ$ grid is converted to a $0.5^\circ \times 0.5^\circ$ grid. It should be note that the snow cover data is not available over high latitudes (north of 60°N) during winter polar night, as the snow cover observations rely on visible light. For all snowpack datasets, a 3-day running mean is applied to fill in the missing data.

According to the main periodicity band determined in Sect. 3, all daily subseasonal anomalies of each variable are obtained by first removing the climatological annual cycle (annual mean plus three leading harmonics) and then a 20–80-day bandpass filtering. Analyses in the following will be conducted for the extended boreal winter from November to March.

2.3 Temperature tendency equation and moisture budget equation

The temperature tendency equation in pressure coordinates is used in Sect. 5.1 to diagnose the key processes that drive the formation of the subseasonal T anomalies, which can be written as (Holton 1973; Hegyi and Deng 2017)

$$\frac{\partial T'}{\partial t} = \left(-u \frac{\partial T}{\partial x} - v \frac{\partial T}{\partial y} \right)' + \left(-\omega \frac{\partial T}{\partial p} + \omega \frac{\alpha}{C_p} \right)' + \left(\frac{\dot{Q}}{C_p} \right)' \quad (1)$$

where α is the specific volume, the specific heat of air C_p , and the rate of diabatic heating \dot{Q} . Primes denote the subseasonal components (20–80 days). The terms on the right-hand side are anomalies of horizontal temperature advection, adiabatic heating related to vertical motion, and diabatic heating, respectively. The diabatic heating term is not directly provided by the ERA5 dataset, so it is calculated as the residual of the temperature tendency equation.

In addition, we use the vertical integral of the moisture budget equation to address the change in precipitation (Johnson and Feldstein 2010; Chou and Lan 2012; Peng et al. 2018):

$$P' = -\frac{1}{g} \langle \partial_t q' \rangle' - \frac{1}{g} \langle \vec{V}_h \cdot \nabla_h q' \rangle' - \frac{1}{g} \langle \omega \partial_p q' \rangle' + E' + R \quad (2)$$

Here, P, E, and q denote precipitation, evaporation, and specific humidity, respectively. The \vec{V}_h is the horizontal vector wind, g is the gravitational acceleration (m s^{-2}), $\langle \rangle$ is the column integration from surface to tropopause, ∂_t and ∂_p denote the time and pressure derivative of variables,

Table 1 The snow depth and cover datasets used in this study

Datasets	Variable	unit	time	Grid resolution	supplement
GlobSnow	snow water equivalent	mm	1979–2018	25 km \times 25km	combined data
MERRA-2	snow depth	m	1980–2022	$0.5^\circ \times 0.625^\circ$	reanalysis data
JRA-55	Snow depth	m	1979–2022	$1.25^\circ \times 1.25^\circ$	reanalysis data
ERA5_Land	Snow depth	m	1979–2022	$0.5^\circ \times 0.5^\circ$	reanalysis data
Modis/Terra	snow cover	%	2000–2022	$0.05^\circ \times 0.05^\circ$	satellite data

respectively, and ∇_h is the horizontal operator. The precipitation anomaly is contributed by four terms: the local change of specific humidity, horizontal and vertical moisture advections, and evaporation. R is the residual term, which is calculated by moisture budget equation.

Precipitation data are obtained from the Climate Prediction Center (CPC) Unified Gauge-Based Analysis of Global Daily Precipitation provided by NOAA (Xie et al. 2007). The horizontal resolution of this precipitation data is $0.5^\circ \times 0.5^\circ$. We estimate evaporation using the Eq.

$$E = LH/\lambda \quad (3)$$

where LH is the surface latent heat flux, and λ is the latent heat of vaporization (MJ kg^{-1}); $\lambda = (2.361 \times 10^{-3}) \times \text{SAT}$, where the unit of SAT is $^\circ\text{C}$ (Allen et al. 1998; Peng et al. 2018).

2.4 Extraction of subseasonal teleconnection indices over mid-high latitudes

The daily Scandinavia (SCAN) index and East Atlantic/West Russia (EAWR) index are obtained by projecting wintertime SCAN and EAWR patterns onto the daily anomalies data. These patterns are the sixth and fourth rotated empirical orthogonal function (REOF) modes of monthly 500-hPa geopotential height (Z500) anomalies over the region 20° - 90°N , 0° - 360°E for winters of 1979–2021, respectively (Liu et al. 2014; Lim 2015; Zhang et al. 2022).

Similarly, the daily Polar/Eurasia (PEU) index is obtained by projecting the first empirical orthogonal function (EOF1) mode onto the daily anomalies data. An EOF analysis is performed on monthly Z500 anomalies over the region 40° - 80°N , 30°W - 130°E for winters of 1979–2021 to get the EOF1 pattern (Jiang et al. 2023).

To extract the subseasonal (20-80-day) signals, a 20-80-day bandpass filtering is applied to daily teleconnection indices, which include SCAN, EAWR, PEU, Arctic Oscillation (AO), and North Atlantic Oscillation (NAO) index. The last two indices are obtained from the National Oceanic and Atmospheric Administration Climate Prediction Center website (<https://www.cpc.ncep.noaa.gov/products/precip/CWlink/pna/nao.shtml>, https://www.cpc.ncep.noaa.gov/products/precip/CWlink/daily_ao_index/ao.shtml).

3 Subseasonal variability of SLP over mid-high-latitude Eurasia

Fig. 1a shows the SLP climatological field over the Northern Hemisphere during boreal winter. Three pronounced atmospheric activity centers are observed over the mid-high

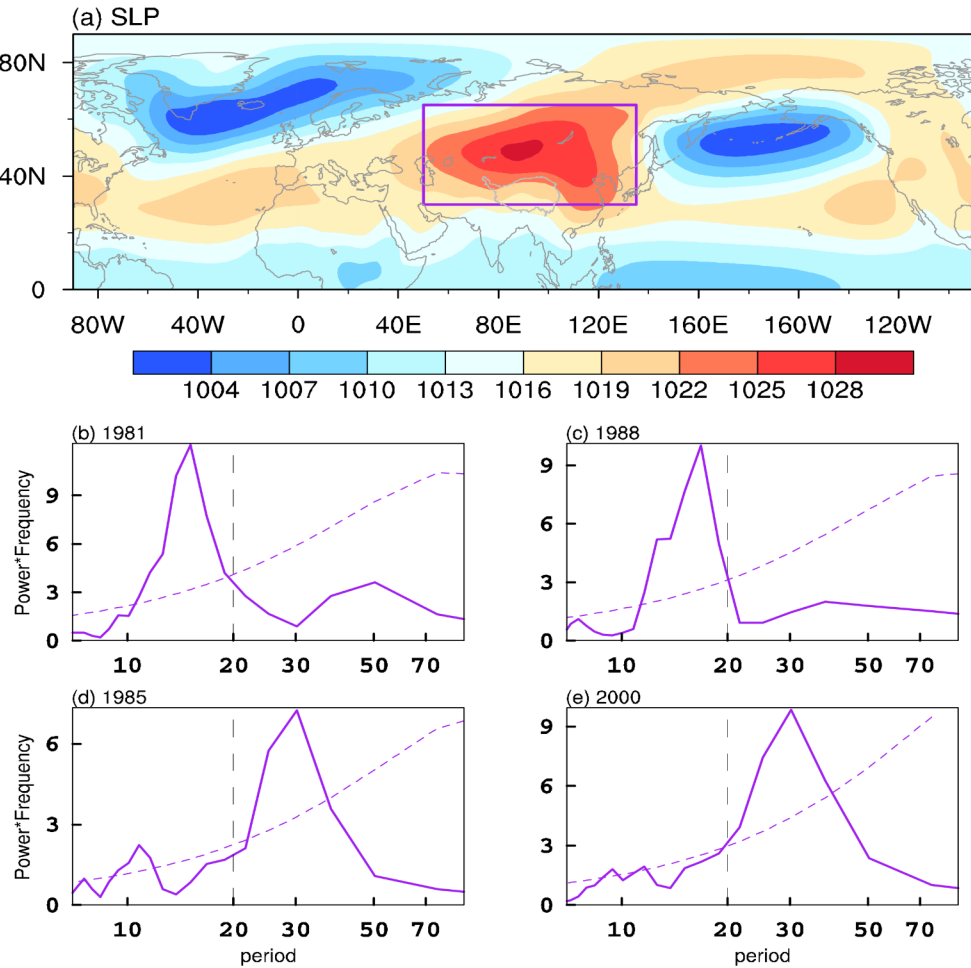
latitudes of the Northern Hemisphere: the Iceland Low near Greenland, the Aleutian Low over the Bering Strait, and the Siberian High over mid-high-latitude Eurasia, respectively.

To investigate the dominant subseasonal periodicity over mid-high-latitude Eurasia, we apply a power spectral analysis on the subseasonal component of SLP over the region of 30° - 65°N , 50° - 135°E (purple box marked in Fig. 1a). Prior to the power spectrum analysis, the perturbations with synoptic time-scale were moved by 5-day running means. Similar to previous studies (Ding 1990; Takaya and Nakamura 2005a), the SLP anomaly has a significant peak between 10 and 20 days in 1981 and 1988 (Fig. 1b, c). Another robust peak more than 20 days can be seen in 1985 and 2000. To clarify the importance of the period more than 20 days, the power spectrums of SLP variability during each individual boreal winter from 1979 to 2021 are shown in Fig. S1. It shows that, besides the significant peak of 10–20 days, a significant period between 20 and 80 days is observed in 20 years. Their peaks range from 20 to 50 days with mean peak about 36 days. According to Llovel et al. 2014, these two period components can account for 27% (10-20-day) and 44% (20-80-day) of the total daily variance of SLP anomaly, respectively. Since our focus is on period longer than 20 days, the 20-80-day band of subseasonal component is selected for this study. The subseasonal anomalies represent 20-80-day filtered components in the following paper unless otherwise stated.

3.1 Evolution characteristics of the leading subseasonal SLP mode

To extract the leading subseasonal SLP variability mode over mid-high-latitude Eurasia, an empirical orthogonal function (EOF) analysis is applied to the 20-80-day filtered SLP anomalies over the region of 30° - 65°N , 50° - 135°E (purple box marked in Fig. 1a) during boreal winters of 1979–2021. Before the EOF analysis, 20-80-day-filtered SLP anomalies were weighted by the square root of the cosine of the latitude, in order to account for the change in the area of a grid cell with latitudes. The first EOF (EOF1) mode explains 47% of the total SLP variance. Figure 2a shows the linear regression of 20-80-day SLP anomaly on the principal component (PC1) time series of the EOF1 (shaded) and SLP climatological field (contours) during boreal winter. The regression of 20-80-day SLP anomaly on the PC1 (Fig. 2a) is consistent with the spatial pattern of the EOF1. The spatial pattern of EOF1 in Fig. 2a demonstrates a monopole of SLP anomalies with anomalous high over the north of 40°N . This anomalous high's center, near the Ural Mountains, is located on the northwest flank of climatological Siberian High center (Fig. 2a). As suggested by power spectra of the first principal component (PC1) of the EOF1,

Fig. 1 (a) SLP climatological field (shaded; hPa) during boreal winter of 1979–2021. The purple box indicates the key domain (30° – 65° N, 50° – 135° E). (b–e) Power spectra (purple solid line) of daily SLP anomaly with 5-day running means averaged over the purple box in Fig. (a) during four individual winters (1981, 1988, 1985, 2000), with the 99% confidence level (purple dotted line). The black dotted lines are the period of 20 days



this leading mode exhibits a prevailing period of 20–50 days with a peak at 36 days (Fig. 2b).

To characterize the propagation and three-dimensional structure of the SLP leading mode, we identify positive and negative events based on the normalized PC1 of SLP EOF1. A positive (negative) event is selected when the normalized PC1 is above (below) the threshold of 1.5 (-1.5) for at least five consecutive days. In each positive (negative) event, the peak day (day 0) refers to the day with the biggest (smallest) PC1. The interval between each peak day was set to more than half period (18 days), which renders the subseasonal period for individual events. With above criteria, a total of 47 positive events and 46 negative events are identified for 43 winters of 1979–2021, as shown in Fig. 2c. The composite analysis of the normalized PC1 indicates that both positive and negative phases last approximately 18 days (Fig. 2d), suggesting a period of 20–50 days for EOF1 (Fig. 2d). This result is consistent with the power spectrum analysis (Fig. 2b). Since the positive event composite is essentially a mirror image of the negative one (Fig. 2d), the next composite results (Figs. 3, 4, 5, 6, 7, 8, 9, 10, 11, 12 and

13) are half the difference between the positive and negative events.

Figure 3 shows lead-lag composites of subseasonal SLP and SAT anomalies based on positive and negative events from days –15 to 12 with a 3-day interval. The composite of SLP anomaly on day 0 assembles the SLP EOF1 pattern. On day –15, a strong surface anomalous low, centered near the Ural Mountains, dominates the mid-high-latitude Eurasia (Fig. 3a). After day –15, the anomalous low moves to East Asia and weakens (Fig. 3a–e). A weak surface anomalous high center appears near the Barents-Kara Sea on day –9 (Fig. 3c). Subsequently, it begins to move southeastward and intensify (Fig. 3c–f). On day 0, the anomalous high gets its peak, with the center located near the Ural Mountains (Fig. 3f). In the following days, the strong anomalous high moves to East Asia and gradually weakens (Fig. 3g–j). On day 9, a weak anomalous low centered near the Barents-Kara Sea is observed (Fig. 3i). This low then moves southeastward and intensifies from day 9 to day 12 (Fig. 3j). The SLP anomalous pattern on day –9 largely mirrors that on day 9 with an opposite sign, further suggesting a period of about 36 days for the leading subseasonal SLP mode.

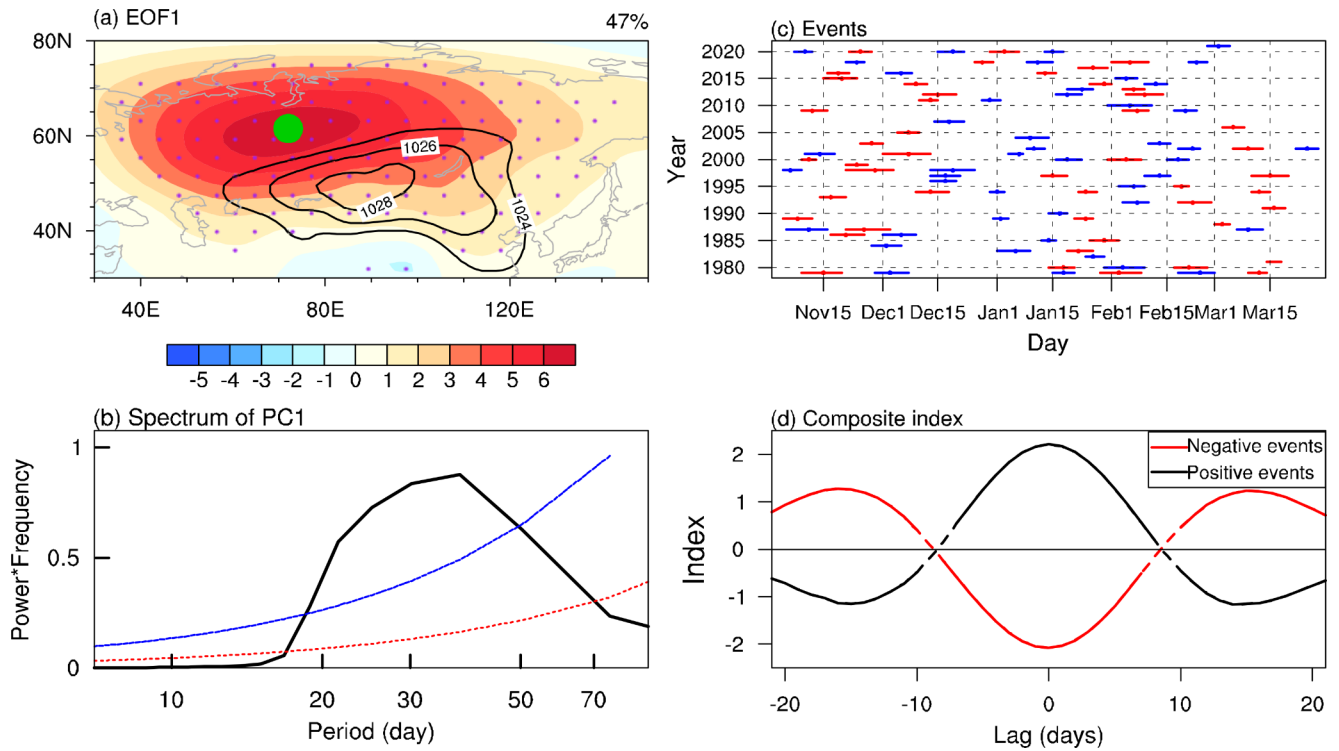


Fig. 2 (a) Regressed 20–80-day subseasonal SLP (shaded; hPa) anomalies against the normalized PC1 during boreal winter. Areas with purple dots indicate SLP anomalies surpassing the 99% significance level. The green dot denotes the center of anomalous high on SLP field. The value at the upper-right corner indicates the percentage of variance explained by the EOF1. Black contours denote the SLP climatological field during boreal winter. (b) Power spectra of the PC1 in winters from 1979 to 2021 (black), with Markov red noise spectrum (red) and

We can see that the surface anomalous high (low) over mid-high-latitude Eurasia is coupled with SAT cold and warm anomalies (Fig. 3). These anomalies are situated on the southeast (northwest) and northwest (southeast) flanks of the anomalous high (low) center throughout the whole evolution. In terms of propagation, the SAT anomalies move southeastward following the surface anomalous high (low; Fig. 3). In addition, it is seen that the positive SLP anomaly near the Ural Mountains get its peak on day 0, coinciding with the coldest anomaly over the Balkhash-Baikal Lake, and it precedes the warmest anomalies over the Barents-Kara Sea by about 3 days. Above relationships suggest that SAT anomalies tend to be driven by surface atmospheric circulation. Consequently, cold (warm) anomalies on the southeast (northwest) flank of surface anomalous high can be due to the cold temperature advections by northerly (southerly) anomalous winds associated with the surface high pressure system on SLP field, as previously noted (e.g., Yang and Li 2016; Lin 2018; Kim et al. 2021; Guan and Wang 2023).

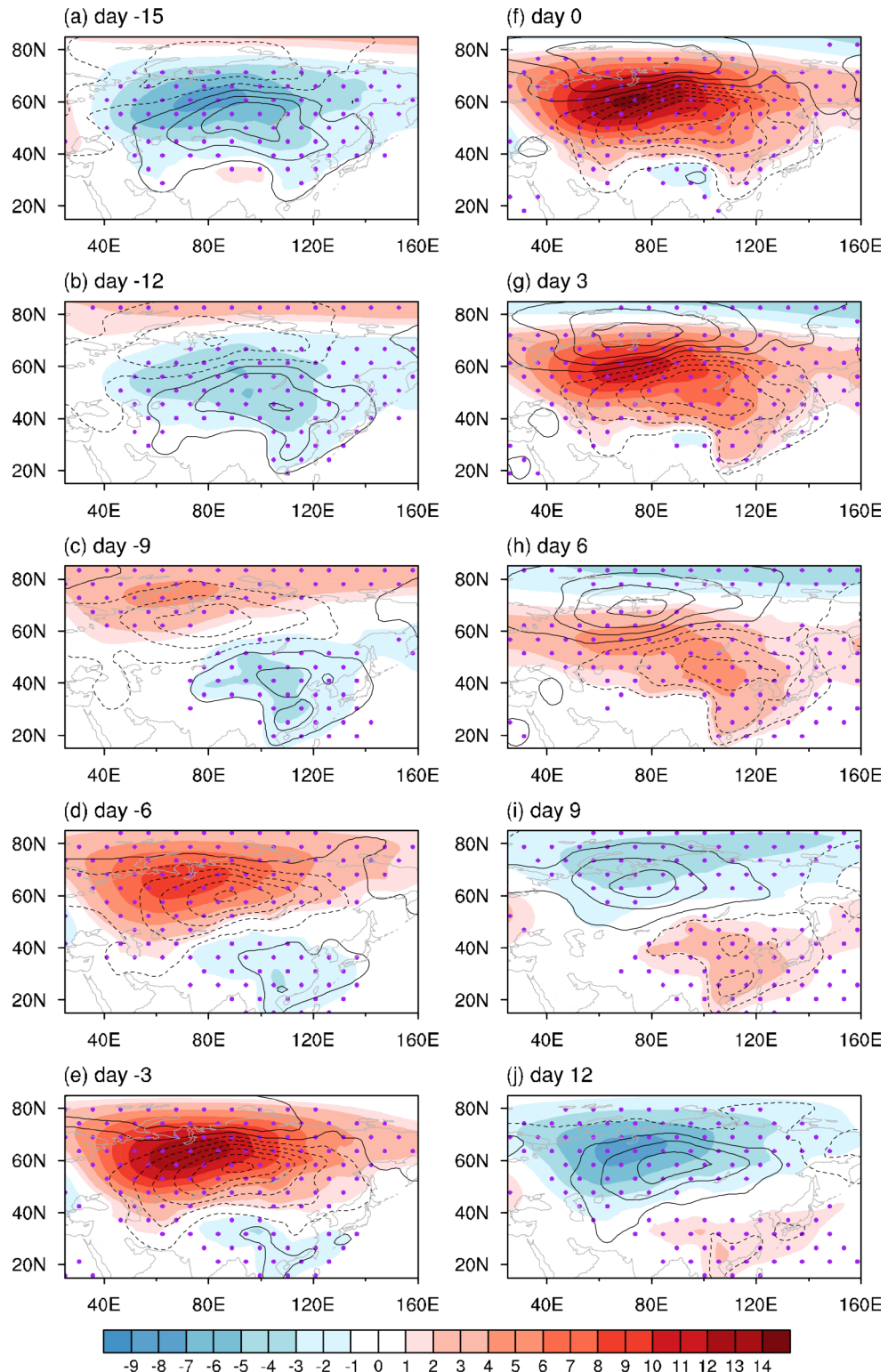
the 99% confidence level (blue). (c) Positive and negative subseasonal events with respect to EOF1 during the winters of 1979–2021. The red (blue) lines denote the positive (negative) events, the dots denote the day 0 of subseasonal events. (d) The lead-lag composite of the normalized PC1 for positive and negative events. The solid (dashed) lines indicate values exceeding (not exceeding) the 95% confidence level based on the Student's t-test

3.2 Vertical structure of the leading subseasonal SLP mode

Figure 4a-d depict the spatial patterns of composited Z and T anomalies at 100 hPa, 300 hPa, 500 hPa and 900 hPa, respectively, on day 0. An equivalent barotropic structure in vertical Z and T anomalies is clearly observed in the troposphere. On day 0, along with surface anomalous high near the Ural Mountains on SLP field in Fig. 3f, strong positive Z anomalies can also be discerned almost over the same region in vertical levels up to the tropopause. Negative T anomalies over the Balkhash-Baikal Lake and positive T anomalies over the Barents-Kara Sea extend from the surface to 300 hPa. Besides, weak negative Z anomalies can also be seen near Western Europe and the Balkhash-Baikal Lake in the mid-upper troposphere.

To show more clearly the vertical structure of Z and T anomalies, Fig. 4e and f depict the latitude-height (averaged over 45°–110°E) and longitude-height (averaged over 45°–75°N) cross sections of composite Z and T anomalies on day 0. Above ranges are selected based on the location of the anomalous high center (the purple box in Fig. 4d).

Fig. 3 Lead-lag composites of subseasonal SLP (shaded; hPa) and SAT (contours start at ± 0.5 K with interval of 1 K, dashed if negative) anomalies. Areas with purple dots indicate SLP anomalies surpassing the 99% significance level. (a-j) from day – 15 to day 12, with interval of 3 days, respectively



In Fig. 4e, a positive (negative) Z anomaly with center at 300 hPa is located north of 60°N (near 45°N). The Z anomalies tilt northwards with increasing height. From the longitude-height profile (Fig. 4f), a positive (negative) Z anomaly with center at 300 hPa is located near 60°E (near 0°E). The

Z anomalies also exhibit a westward tilt with increasing height. In terms of T anomalies, below (above) the positive Z anomaly center, the T shows a warm (cold) anomaly, following well the hydrostatic relationship.

Fig. 4 Composites of subseasonal Z (shaded; gpm) and T (contours; K) anomalies at levels of (a) 100 hPa, (b) 300 hPa, (c) 500 hPa and (d) 900 hPa on day 0; The purple boxes in (b-d) indicates the region (50° – 85° N, 35° – 85° E), (50° – 85° N, 40° – 85° E), and (45° – 75° N, 45° – 110° E), respectively. (e) Latitude-height cross section of composite subseasonal Z (shaded; gpm) and T (contours; K) anomalies averaged over 45° – 110° E on day 0. (f) As in (e), but for longitude-height cross section average over 45° – 75° N. (g) Lead-lag correlation coefficients between PC1 and Z anomalies averaged over the box region in Fig. (b) at 300 hPa and over the box region in Fig. (c) at 500 hPa. A negative lag denotes Z anomalies leads PC1. The solid lines indicate values exceeding the 95% confidence level based on the Student's t-test

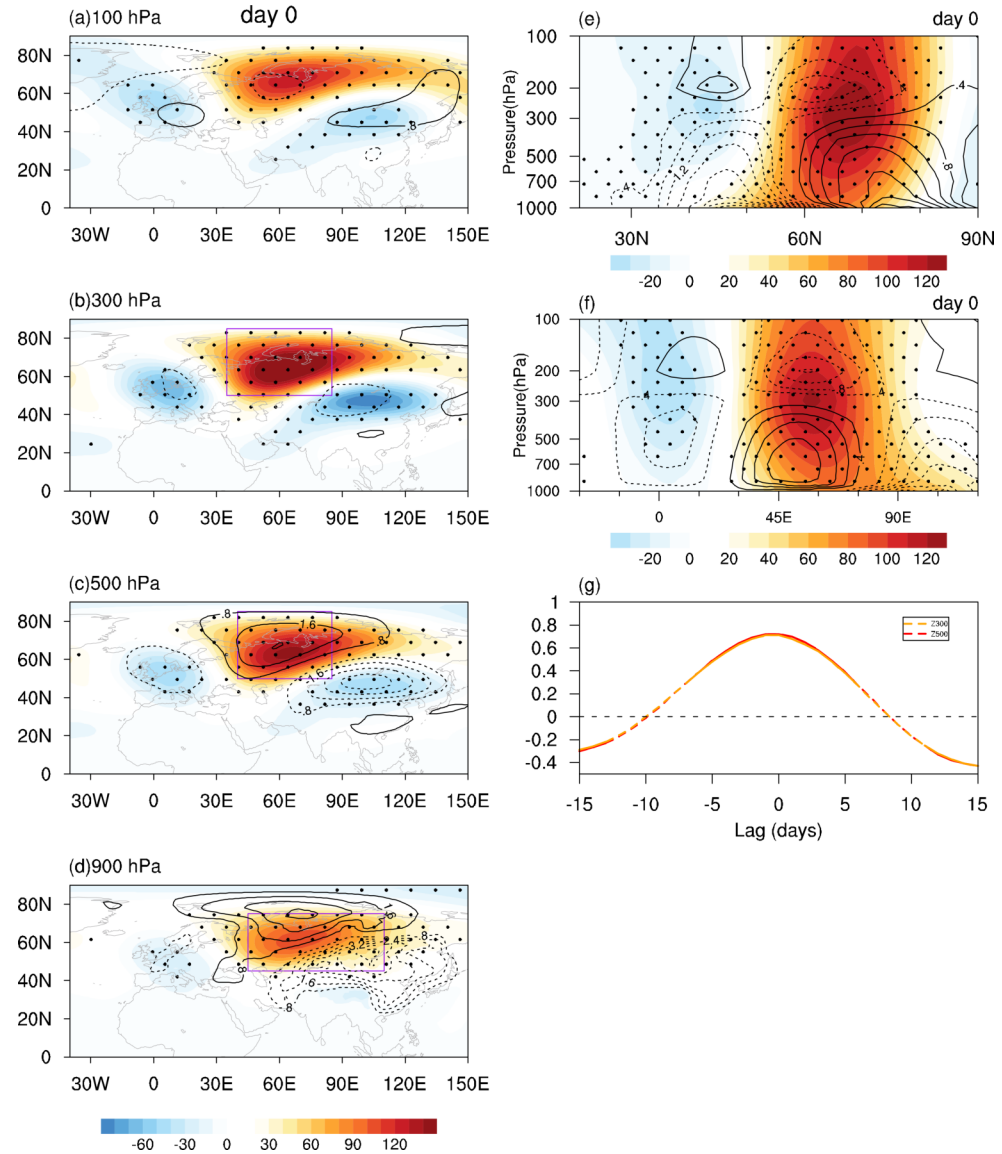
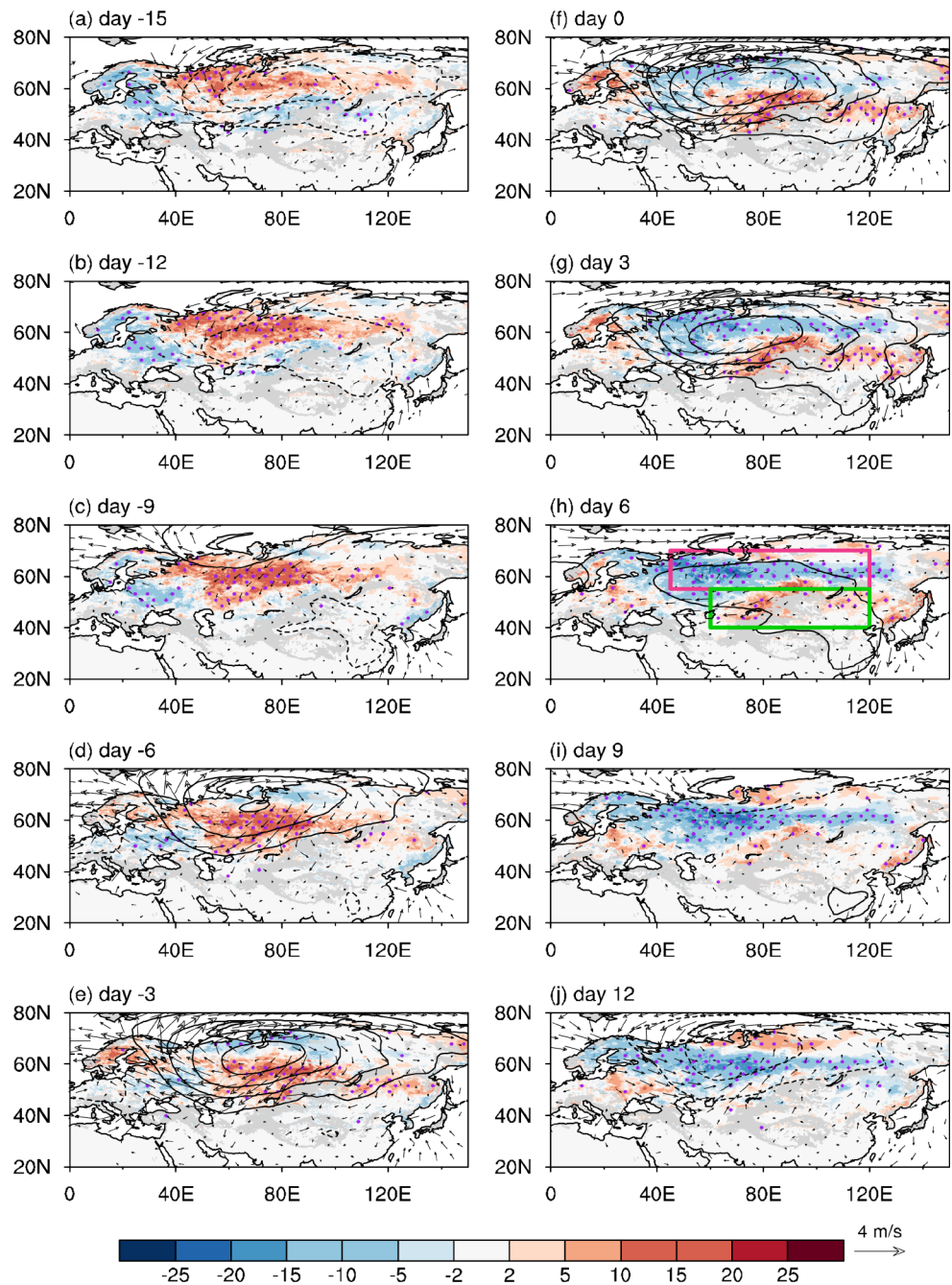


Figure 4g shows the lead-lag correlation between PC1 and Z anomalies over the critical areas at 300 and 500 hPa (the purple boxes in Fig. 4b, c), respectively. When the indices for Z anomalies in the mid-upper troposphere lead PC1 by 1–2 days, the correlations reach the maximum. It implies the anomalous blocking ridge can reinforce the anomalous high at the surface, by (1) inducing anomalous cold advection and (2) as a component of a quasi-stationary Rossby wave train propagating the Eurasian continent under modest feedback from eddy forcing (Takaya and Nakamura 2005a, b; Bueh and Xie 2015).

4 Snowpack anomalies associated with the leading subseasonal SLP mode

Our calculation showed that, the climatological SD over mid-high-latitude Eurasia is about 20 cm (Figure omitted). The subseasonal SD anomaly, linked to the leading SLP mode, can reach about ± 2.5 cm. This value is about 25% of the local climatological value. Figure 5 shows lead-lag composites of subseasonal SD, SLP and surface wind anomalies, associated with the SLP mode, over mid-high-latitude Eurasia based on the GlobSnow dataset. Corresponding to the surface anomalous system over mid-high-latitude Eurasia on SLP field, positive SD anomalies are observed over the southeast flank of the anomalous high center and over the northwest flank of the anomalous low center. Conversely, negative SD anomalies are observed over the northwest flank of the surface anomalous high center and over

Fig. 5 Lead-lag composites of subseasonal SD (shaded; mm; GlobSnow), SLP (contours with interval of 3 hPa; dashed if negative; zero contours omitted) and 10 m surface wind anomalies. The purple dots denote SD anomalies significant at the 95% confidence level. The pink box in (h) indicates the region of 55°–70°N, 45°–120°E, the green box in (h) indicates the region of 40°–55°N, 60°–120°E. (a–j) from day –15 to day 12, with interval of 3 days, respectively

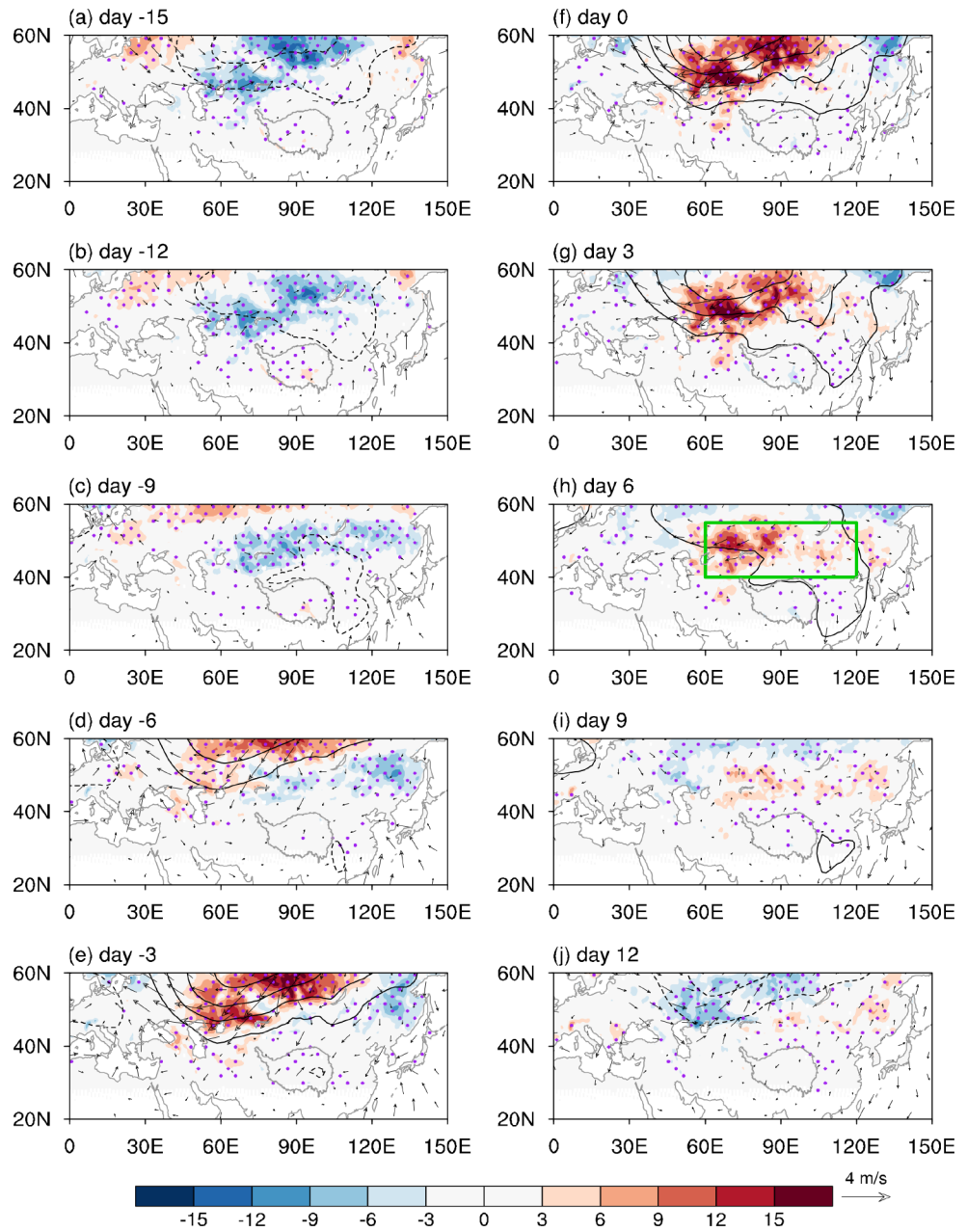


the southeast flank of the anomalous low center (Fig. 5). These SD anomalies propagate southeastward following the surface anomalous high (low). Similar to previous studies (Song and Wu 2019; Song et al. 2019b), positive SD anomalies are associated with northerly wind anomalies which lead to the SAT cold anomalies. Negative SD anomalies are associated with southerly wind anomalies which lead to the SAT warm anomalies.

The SD anomalies associated with the leading SLP mode over mid-high-latitude Eurasia in the three reanalysis datasets (JRA-55, MERRA-2 and ERA5_Land) show a similar

distribution and propagation (Figures S2–S4). There are some differences in the amplitude and regional spatial distribution between the GlobSnow dataset and the three analysis datasets. For example, the amplitude of SD anomalies is overestimated in ERA5_Land (Figure S4), which is attributed to the assimilation of observed snow data (Komatsu et al. 2023). Another noticeable difference in SD anomalies is observed near 30°N over East Asia based on MERRA-2 datasets (Figure S3). This difference is due to the fact that the standard deviation field based on MERRA-2 dataset

Fig. 6 As in Fig. 5, but for the subseasonal SC anomaly (shaded; %)



shows pronounced subseasonal SD variability over East Asia, unlike other datasets (Figure S5).

Figure 6 shows lead-lag composites of subseasonal SC, SLP and surface wind anomalies, associated with the SLP mode, over mid-high-latitude Eurasia. It is seen that, SC anomalies over mid-high-latitude Eurasia are also closely associated with the leading subseasonal SLP mode. The SC anomalies display a robust southeastward propagation. Positive (negative) SC and northerly (southerly) wind anomalies are observed over the southeast flank of surface anomalous high (low) on SLP field (Fig. 6a, f). Above SC anomalies move from the Balkhash-Baikal Lake to Northeast Asia following the southeastward propagation of the

surface anomalous system. In terms of amplitude, the positive SC anomalies reach the peak on day 0. Then they start to weaken.

The above analysis reveals that the SD and SC anomalies present significant evolution characteristics when southeastward-propagating leading SLP mode across mid-high-latitude Eurasia. To further understand the relationship between the leading SLP mode and snowpack (SD and SC) anomalies, in the next section, we elaborate it from the possible mechanisms for snowpack's formation.

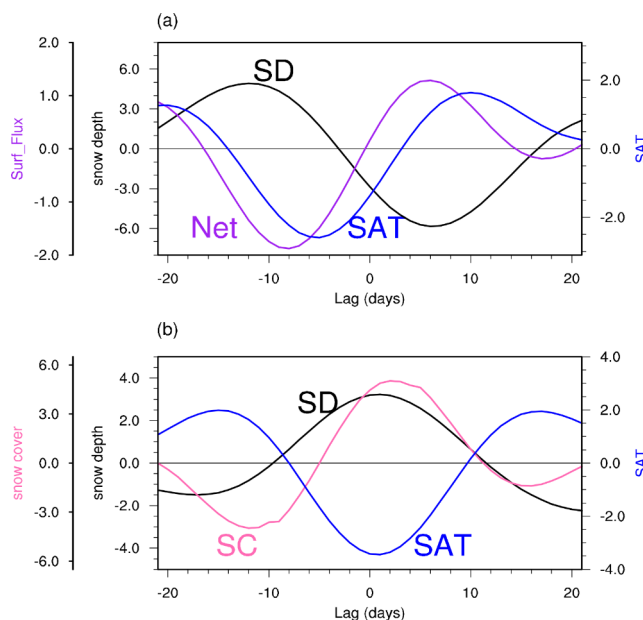


Fig. 7 (a) Time evolution of composite regional mean SAT (blue curve; K), SD (black curve; mm) and net energy flux (purple curve; $W \cdot m^{-2}$) anomalies over the high latitude region (pink box in Fig. 5h). (b) As in (a), but for the middle latitude region (green box in Fig. 5h). SC anomaly (pink curve; %/day) over the middle latitude region is also plotted in (b)

5 Physical mechanisms

5.1 Surface air temperature

We demonstrate firstly the lead-lag relationship between subseasonal SAT and snowpack anomalies. Figure 7 depicts time evolution of SAT, SD and SC over the high latitude region (55° - 70° N, 45° - 120° E; the pink box in Fig. 5h) and middle latitude region (40° - 55° N, 60° - 120° E; the green box in Fig. 5h), respectively. It is seen that there is a difference in the lead-lag relationship between SAT and SD anomalies over the high latitude region and middle latitude region. Over the high latitude region (55° - 70° N, 45° - 120° E; the pink box in Fig. 5h), the maximum SD anomaly is observed on about day -11, and the minimum net energy flux and SAT anomalies can be seen on day -9, -5, respectively (Fig. 7a). This lead-lag relationship indicates that increased snow depth can also influence surface air temperature (SAT) anomaly through land surface energy flux.

Table 2 shows the surface energy flux anomalies over the high latitude region (pink box in Fig. 5h) from day -10 to day -6. We can see that the following three physical processes influence the SAT cold anomaly: (1) the decreased sensible heat flux can gradually cause the cold anomaly of the surface air, due to thermal insulation effect of snow depth (Lynch-Stieglitz 1994; Stieglitz et al. 2001; Li et al. 2018). (2) Due to the clear sky associated with anomalous high on

SLP field from day -10 to day -6, the downward longwave radiation decreases. This contributes to a decreased net longwave energy and the surface cold anomaly finally. (3) The downward shortwave radiation received by the surface increases, due to the clear sky. While snow-albedo effect offsets some of the received shortwave radiation, indicating a decreasing effect on SAT.

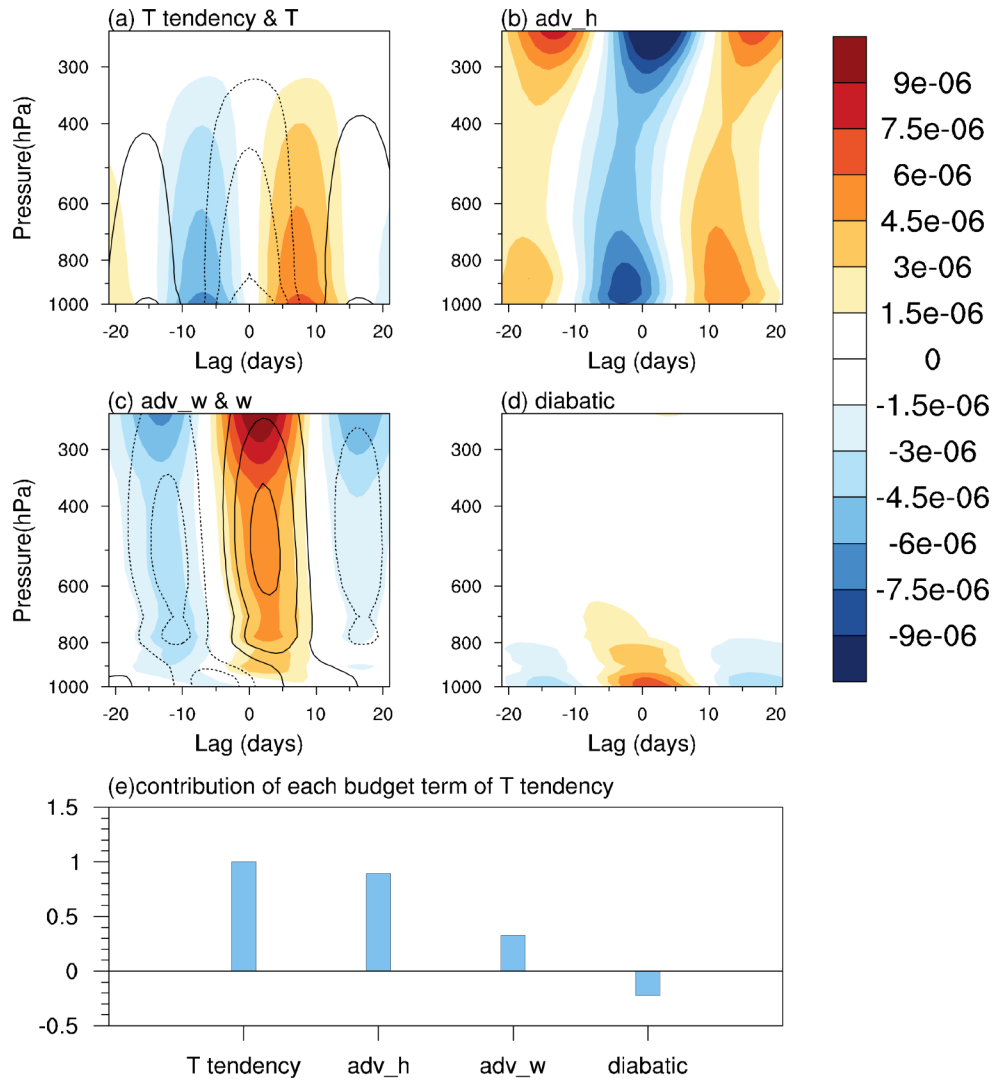
Over the middle latitude region (40° - 55° N, 60° - 120° E; the green box in Fig. 5h), the negative SAT anomaly leads the positive SD anomaly by about 1 day, and it leads the positive SC anomaly by about 3 days. These relationships mean that the influence of SAT anomaly on snowpack mainly occur over the middle latitude region, not over the high latitude region. To further elucidate the dominant processes contributing to the temperature anomalies over the middle latitude region, the temperature tendency equation is diagnosed. Figure 8a-d show the time-height evolutions of temperature (T), T tendency anomalies, horizontal term (adv_h), adiabatic heating (adv_w) and diabatic heating term over the middle latitude region. The cold anomalies extend from the surface to the upper troposphere, and exhibit a decreasing amplitude with increasing height (Fig. 8a) near day 0. Strong negative and positive T tendencies are observed before and after day 0, respectively. These tendencies are primarily driven by horizontal temperature advection (Fig. 8b). The adiabatic process matches well with vertical velocity (Fig. 8c). There are cold anomalies at the surface over middle latitude region on day 0. It indicates that an anomalous low, accompanied by upward motion, has passed through this region before day 0, and an anomalous high, accompanied by downward motion, will pass after day 0. Anomalous upward motion results in adiabatic cooling, and anomalous downward motion results in adiabatic warming. Thus, it is suggested that the adiabatic process may influence the T tendency as a trigger due to vertical motion. Diabatic heating makes a minor trigger for air temperature tendency near the surface. (Fig. 8d).

Fig. 8e depicts the contributions of the aforementioned processes to the T tendency. Each of the above processes in the time-height cross section is projected onto the T tendency. Consistent with the above results, horizontal temperature advection plays a dominant role in the evolution of SAT anomalies, accounting for 90% of the ratio. The adiabatic process contributes 33% to the T tendency, while diabatic heating cancels horizontal temperature advection and adiabatic heating, reaching nearly -23% of the T tendency due to lead-lag relationship.

5.2 Snowfall conditions

Snowfall conditions include moisture and vertical motion. On subseasonal time scale, anomalous water vapor flux

Fig. 8 (a-d) Time-height evolution of (a) T tendency (shaded; K/s) and T anomalies (contours with interval of 1 K; dashed if negative; zero contours omitted), and (b) horizontal advection, (c) vertical advection (shaded) and vertical velocity (contours with interval of 0.003 Pa/s; dashed if negative; zero contours omitted), and (d) diabatic processes averaged over middle latitude region (green box in Fig. 5h). (e) Contributions of each T tendency term to the total T tendency calculated by projection coefficient of its spatial pattern (Figs. b-d) onto the total T tendency pattern over the time-height cross section (Fig. a) between day-15 and day 0



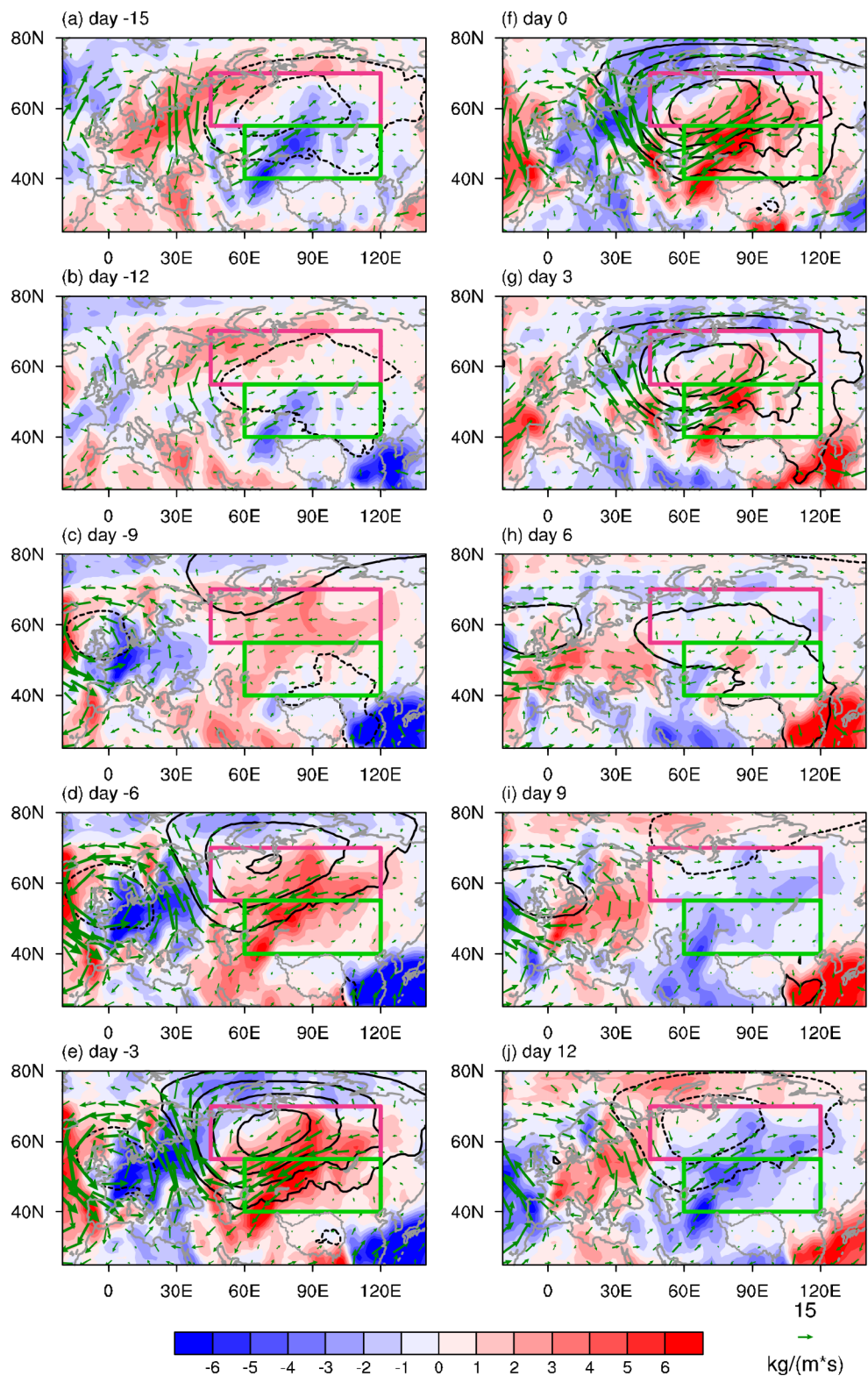
convergence (divergence) and upward (downward) motion result in positive (negative) snowfall anomalies.

Figure 9 shows the evolution of anomalous water vapor flux and its divergence associated with the leading subseasonal SLP mode. Along with the surface anomalous high (low) moving from the Barents-Kara Sea to East Asia on SLP field, there is also a southeastward propagation of anomalous anticyclonic (cyclonic) water vapor transportation from the Barents-Kara Sea to East Asia. Anomalous water vapor flux divergence is situated on the southeast (northwest) flank of the anticyclone (cyclone) center. The anomalous convergence is located on the northwest (southeast) flank of the anticyclone (cyclone) center. Meanwhile, a wave train originating from the subtropical North Atlantic can be noticed from the water vapor flux in Fig. 9. This indicates that this wave train is conducive to the transport of water vapor which leads to the formation of snowfall. We will discuss this wave train further in Sect. 5.3.

Figure 10 illustrates the vertical motion at 500 hPa associated with the leading SLP mode. It is observed that the anomalous vertical motion also features a pronounced southeastward propagation from the Barents-Kara Sea to East Asia during the whole evolution. The anomalous downward (upward) motion at 500 hPa is located on the southeast flank of the surface anomalous high (low) center on SLP field. The spatial distributions above demonstrate that the anomalous water vapor flux convergence and upward motion, associated with the evolution of the SLP anomaly, both occur almost over the same region, and contribute to the local snowfall anomaly.

To better understand the temporal relationship between snowpack anomalies and snowfall atmospheric condition anomalies, we present the evolution of regional anomalous snowpack tendency, water vapor divergence integrated from 1000 to 100 hPa and vertical velocity at 500 hPa associated with the subseasonal SLP anomaly in Fig. 11. The snowpack tendency is calculated using central differentiation. Over the

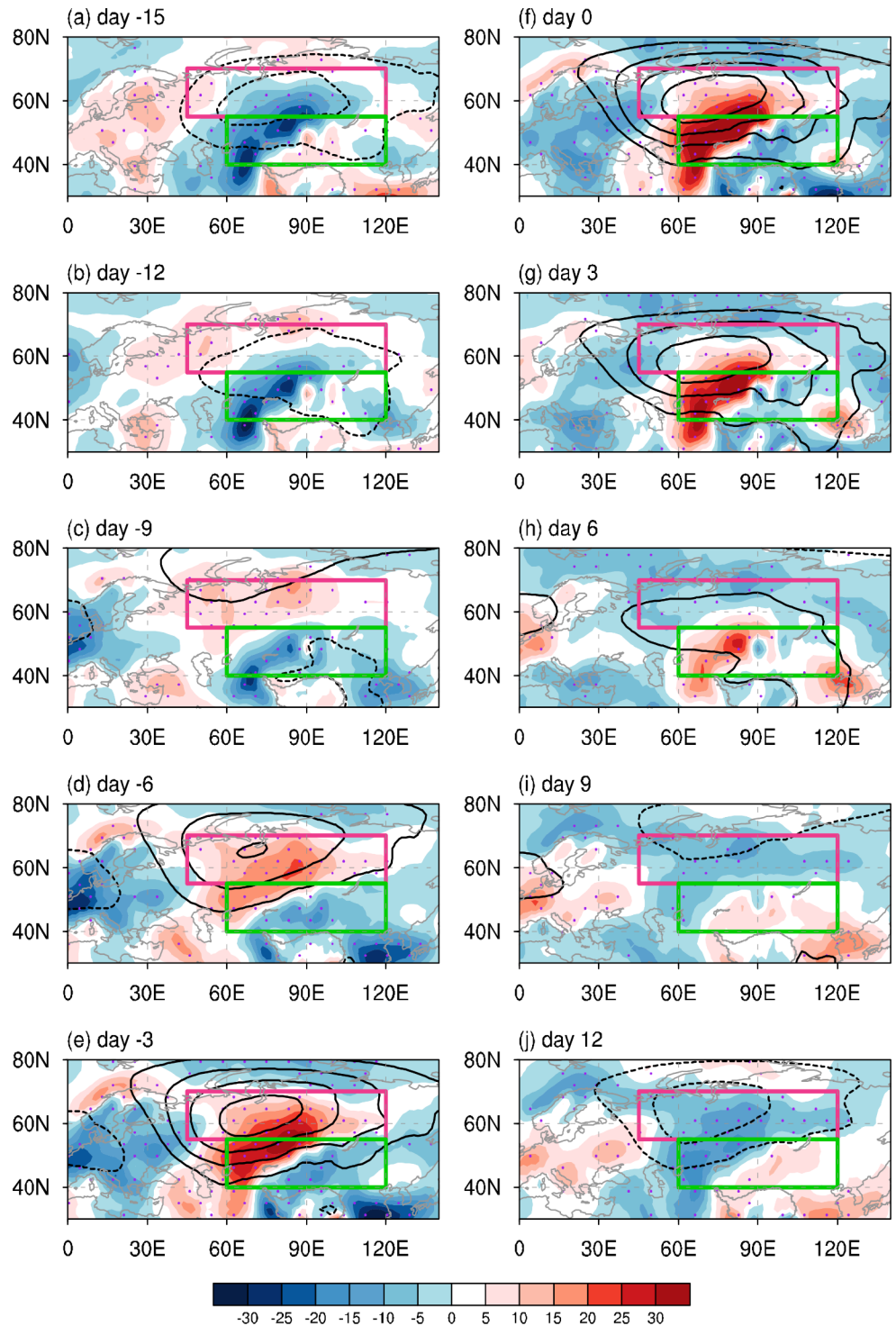
Fig. 9 As in Fig. 5, but for the subseasonal water vapor flux integrated from 1000 to 100 hPa (vector; $kg\ m^{-1}s^{-1}$; scale at right bottom), its divergence (shaded; $\times 10^{-6}kg\ m^{-2}s^{-1}$) and SLP (contours with interval of 3 hPa; dashed if negative; zero contours omitted) anomalies



high latitude region (Fig. 11a), before day -15 , anomalous water vapor convergence and ascending motion contribute to the positive snowfall anomaly, which leads to the positive SD tendency. A weak anomalous water vapor divergence

and descending motion are observed on day -13 , suggesting the negative snowfall anomalies. On day -11 , the snow depth tendency turns to negative from positive, which corresponds to the decrease of positive SD anomalies after day

Fig. 10 As in Fig. 5, but for the subseasonal vertical velocity at 500 hPa (shaded; $\times 10^{-3} \text{ Pa/s}$) and SLP (contours with interval of 3 hPa; dashed if negative; zero contours omitted) anomalies



–11 (Fig. 7a). After day 4, the anomalous water vapor divergence turns to convergence, and descending motion turns to ascending motion. This indicates the snowfall anomalies turn to positive and snow accumulation occurs. As a result, the SD tendency turns from negative to positive on day 7. Furthermore, Fig. 11a shows that snowfall anomalies lead

the SD tendency by 2 days over the high-latitude region, considered as a rapid snowfall accumulation effect.

Over the middle latitude region (Fig. 11b), anomalous water vapor convergence and ascending motion are observed before day –17, indicating positive snowfall anomalies. The SD (SC) tendency becomes positive on day –17 (day –12), which corresponds to the decrease of negative SD

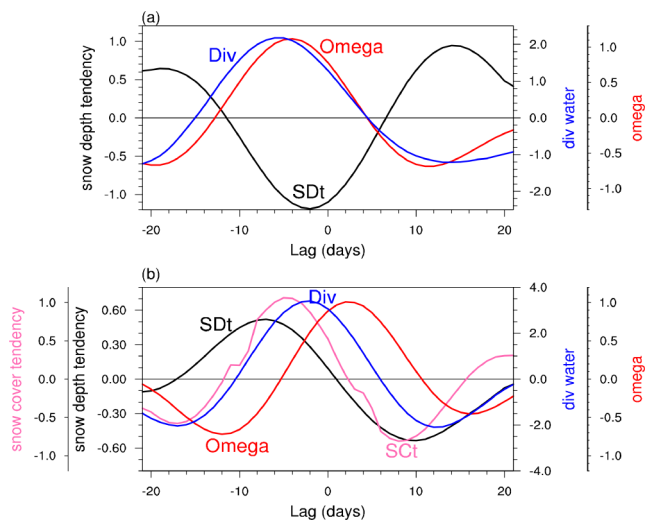


Fig. 11 (a) Time evolution of composite regional mean SD tendency (black curve; mm/day), vertical velocity at 500 hPa (red curve; $\times 10^{-3} \text{ Pa s}^{-1}$) and divergence of water vapor flux integrated from 1000 to 100 hPa (blue curve; $\times 10^{-6} \text{ kg m}^{-2} \text{ s}^{-1}$) anomalies over the high latitude region (pink box in Fig. 5h). (b) As in (a), but for the middle latitude region (green box in Fig. 5h). SC tendency anomaly (pink curve; %/day) over the middle latitude region is also plotted in (b)

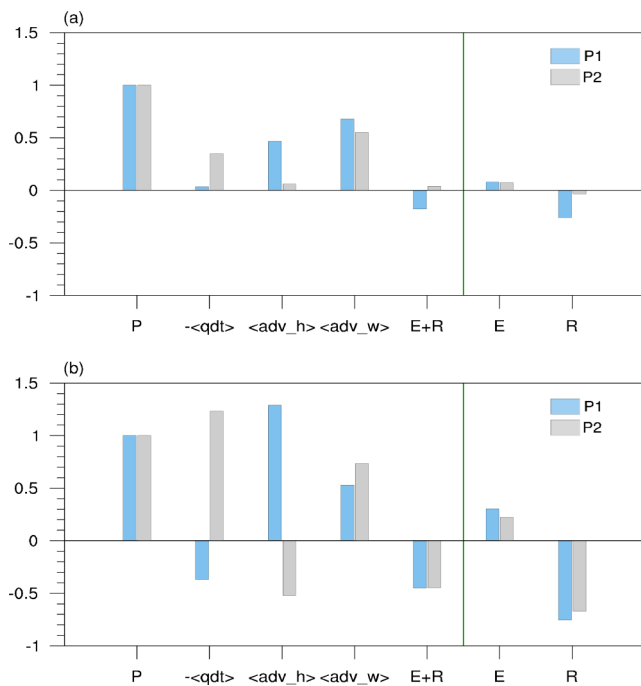


Fig. 12 (a) Contributions of different terms to snowfall anomalies calculated by projection coefficient onto the snowfall anomalies in increasing period (P1; day -11 to day -3; blue bars) and decreasing period (P2; day -3 to day 6; gray bars) over high latitude region (pink box in Fig. 5h). (b) As in (a), but for the middle latitude region (green box in Fig. 5h). The blue and gray bars denote the results in increasing period (P1; day -5 to day 2) and decreasing period (P2; day 2 to day 10)

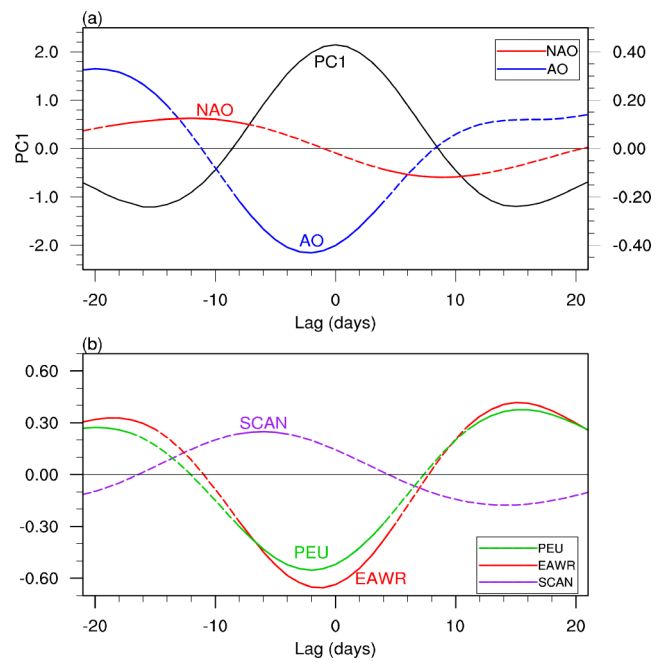


Fig. 13 (a) Time evolution of composite NAO (red curve), AO (blue curve) and PC1 (black curve) index. (b) Lead-lag correlation coefficients between PC1 and SCAN (purple curve), EAWR (red curve) and PEU (green curve) indices. A negative lag denotes the circulation index leads PC1. The solid lines indicate values exceeding the 95% confidence level based on the Student's t-test. NAO = North Atlantic Oscillation; AO = Arctic Oscillation; SCAN = Scandinavian Pattern; EAWR = East Atlantic/West Russia pattern; PEU = Polar/Eurasia pattern

after day -17 (day -12; Fig. 7b). Besides, the water vapor turns to divergence on day -10, followed by a transition from anomalous upward to downward motion on day -5. Above signals mean the negative snowfall anomalies after day -5. Next, the SD (SC) tendency turns to negative on day 0 (day 2), which corresponds the decrease of positive SD (SC) anomalies after day 0 (day 2; Fig. 7b). Furthermore, it is evident that SD anomaly responds more quickly to atmospheric condition than the SC anomaly by 2–5 days over the middle latitude region. The possible reasons about the lead-lag relationship are discussed in Sect. 6.

Figure 12 illustrates the contributions of different processes to the snowfall anomaly through the moisture budget equation. Based on the snowfall anomaly, the increasing period (P1) refers to the period when the snowfall anomaly reaches its peak from zero value of snowfall anomaly. The decreasing period (P2) refers to the period when the snowfall anomaly reaches zero value of snowfall anomaly from its peak. Thus, the increasing period is day -11 to day -3, and the decreasing period is day -3 to day 6 over the high latitude region. The increasing period is day -5 to day 2, and the decreasing period is day 2 to day 10 over the middle latitude region (Figure omitted). Over the high latitude region (Fig. 12a), the snowfall anomaly is mainly influenced

Table 2 The surface flux anomalies over the high latitude region on day – 10 to day – 6. The unit of surface flux is $\text{W} \cdot \text{m}^{-2}$. $\downarrow SW$, $\downarrow LW$, $\uparrow SW$, $\uparrow LW$, NetSW, NetLW, SH, LH represent downward shortwave radiation, downward longwave radiation, upward shortwave radiation, upward longwave radiation, net shortwave radiation, net longwave radiation, sensible heat flux and latent heat flux at the surface over the high latitude region, respectively

$\downarrow SW$	$\downarrow LW$	$\uparrow SW$	$\uparrow LW$	NetSW	NetLW	SH	LH
0.69	-9.0	0.39	-8.1	0.29	-0.9	-1.45	0.28

by the vertical transportation of water vapor during the all period. The secondary impact factor is the horizontal water vapor advection during the increasing period (day – 11 to day – 3), while the secondary impact factor is the tendency of water vapor during the decreasing period (day – 3 to day 6). Over the middle latitude region (Fig. 12b), the snowfall anomaly is mainly influenced by the horizontal water vapor advection and secondary by vertical transportation during the increasing period (day – 5 to day 2). During the decreasing period (day 2 to day 10), the tendency of water vapor plays a leading role in snowfall anomalies. The horizontal advection weakens the snowfall anomaly.

5.3 Atmospheric teleconnections over mid-high latitudes

Fig. 13a shows the evolution of subseasonal NAO, AO and PC1 associated with the leading SLP mode. The AO is in negative phase before day 0, and reaches its peak on day – 3. This relationship suggests that the negative AO can rapidly trigger wave trains over mid-high-latitude Eurasia. Above wave trains induce the development of surface anomalous high on SLP field. In comparison, the NAO signal is relatively weaker.

The local atmospheric teleconnections over mid-high-latitude Eurasia are also considered in this study. The lead-lag correlations between three teleconnection indices (EAWR, PEU and SCAN) and PC1 are shown in Fig. 13b. When the EAWR (PEU) leads the PC1 by 8 days, a significant negative correlation is observed. The correlation between EAWR (PEU) and PC1 reaches its peak on day – 2, with a value of -0.65 (-0.55). As the pattern of EAWR is similar to that of PEU (Jiang et al. 2023), the correlation coefficient between these two and PC1 is notably close. The positive correlation between SCAN and PC1 gets its peak when the former leads the latter by 6 days. However, compared to the correlation between the above two atmospheric teleconnection indices and PC1, the correlation coefficient between SCAN and PC1 is much smaller.

6 Summary and discussion

The present study aims to investigate the features of 20–80-day subseasonal SLP variability over mid-high-latitude Eurasia and its influence on snowpack during boreal winter by using the ERA5 atmospheric data and various snowpack datasets. The leading mode of subseasonal SLP variability is examined by performing an EOF analysis over the region $30^{\circ}\text{--}65^{\circ}\text{N}$, $50^{\circ}\text{--}135^{\circ}\text{E}$. Based on the PC1 of the EOF1, a total of 47 (46) positive (negative) events are identified for the winters of 1979–2021. The lead-lag composite analyses are carried out to describe the evolution of the leading SLP mode, and its connection with snowpack. The physical processes associated with atmosphere-snow relationship are revealed.

The leading 20–80-day subseasonal SLP mode exhibits a monopole pattern with an anomalous surface high (low) over mid-high-latitude Eurasia. Its center is located near the Ural Mountains. The PC1 has a significant periodicity of 20–50 days with a peak at 36 days. The above leading SLP mode demonstrates a southeastward propagation from the Barents-Kara Sea to East Asia. It is not confined to the near-surface, but extends deep into the troposphere, with a center at 300 hPa. The geopotential height anomalies exhibit a quasi-barotropic vertical structure, and slop to the northwest with increasing height.

The leading mode shows a strong connection with snowpack anomalies over mid-high-latitude Eurasia. Corresponding to the surface anomalous high on SLP field, positive (negative) SD anomalies are observed on the southeast (northwest) flank of the anomalous high center. An opposite case can also be seen around the surface anomalous low on SLP field. The SD anomalies gradually shift southeastward from the Ural Mountains to Northeast Asia following the movement of the surface anomalous high (low). Similarly, positive (negative) SC anomalies can also be seen over the southeast flank of the anomalous high (low). South of 60°N , the SC anomalies propagate from the north of the Balkhash-Baikal Lake to Northeast Asia, following the movement of the surface anomalous high (low) on SLP field.

The relationship between SAT and snowpack anomalies in situ, accompanied by the leading SLP mode, shows regional characteristics. Over the high latitude region ($55^{\circ}\text{--}70^{\circ}\text{N}$, $45^{\circ}\text{--}120^{\circ}\text{E}$), positive SD anomaly contributes to the SAT cold anomaly through snow-insulation effect, reduced

longwave radiation and snow-albedo effect. Over the middle latitude region (40° - 55° N, 60° - 120° E), the SAT cold anomaly acts as an early cold condition and causes the positive snowpack anomaly in situ.

Snowfall circulation anomalies, associated with the leading SLP mode, contribute to the tendency of snowpack anomalies in situ over the high and middle latitude region. The anomalous convergence of water vapor flux and ascending motion, located on the southeast (northwest) flank of the anomalous low (high) center on SLP field, lead to a positive snowfall anomaly. This results in the snowpack tendency anomaly turning positive. Over the high latitude region, the vertical transportation of water vapor plays a dominant role during snowfall period. Over the middle latitude region, the horizontal water vapor advection plays a leading role during the increasing snowfall period, while the tendency of water vapor plays a primary role during decreasing snowfall period. It is worthy to note that the response of SD is earlier than SC by 2–5 days over the middle latitude region.

We also investigate the relationship between teleconnections (e.g., AO, NAO, SCAN, EAWR, and PEU) and SLP over Eurasia on 20-80-day time scale. When AO, EAWR and PEU are in their negative phases, wave trains are triggered over mid-high-latitude Eurasia. These wave trains can lead to the development of surface anomalous high over Eurasia on SLP field. By modulating the leading subseasonal SLP mode, these atmospheric teleconnections over mid-high latitudes of the Northern Hemisphere may influence snowpack anomalies over mid-high-latitude Eurasia.

This study focuses on examining the influence of the leading 20-80-day subseasonal SLP mode on snowpack over mid-high-latitude Eurasia during boreal winter. It is shown that, the response of snow depth to the leading subseasonal SLP mode occurs 2–5 days earlier than the response of snow cover to the same mode over the middle latitude region. We suggest two possible reasons: (1) The atmospheric circulation related with the leading subseasonal SLP mode can directly influence the snow depth anomaly. If there is large amount of preexisting snow, a large change in snow depth could result in a little change in snow cover (Jeong et al. 2013). When the atmospheric circulation begins to move, the snow cover will be influenced due to its physical attribution during winter. (2) The lag relationship between SD and SC is related to the moving speed of circulation. The average southward propagation speed is 2.5° latitude per day along 60° - 120° E. As the circulation moves southward after three days (for example, from day 0 to day 3 of PC1), it passed through half the middle latitude region, and SC anomaly begins to become significant at this time. Therefore, SC anomaly lags SD anomaly by about 3 days. Further work is needed to verify above two reasons. Besides, this study indicates that EAWR and PEU can modulate

the leading subseasonal SLP mode through wave trains. It is worth noting that both teleconnections are significantly linked to the Atlantic (Liu et al. 2014; Lim 2015; Jiang et al. 2023). Therefore, it is important to explore the relationship between the leading subseasonal SLP mode and the air-sea system in the Atlantic region.

Supplementary Information The online version contains supplementary material available at <https://doi.org/10.1007/s00382-024-07345-5>.

Acknowledgements We thank the two anonymous reviewers for their helpful comments and constructive suggestions, which have greatly improved this paper. This work is supported by the National Key R&D Program of China (2022YFE0106600), and the National Natural Science Foundation of China (42175021).

Funding The National Key R&D Program of China (2022YFE0106600); The National Natural Science Foundation of China (42175021).

Data availability The ERA5 reanalysis data and ERA5_Land snow depth data can be taken from the websites: <https://www.ecmwf.int/en/forecasts/dataset/ecmwf-reanalysis-v5>; <https://www.ecmwf.int/en/forecasts/dataset/ecmwf-reanalysis-v5-land>. The GlobSnow v3.0 snow water equivalent data can be downloaded at https://www.globsnow.info/swe/archive_v3.0/. The MERRA-2 snow depth can be available from https://disc.gsfc.nasa.gov/datasets/M2T1NXLND_5.12.4/summary?keywords=MERRA2%20tavg1_2d_lnd_Nx. The JRA-55 snow depth can be acquired from <https://rda.ucar.edu/datasets/ds628.0/>. The snow cover data can be obtained from the National Snow and Ice Data Center at <https://nsidc.org/data/mod10c1/versions/61>. The daily CPC precipitation data can be assessed at <https://psl.noaa.gov/data/gridded/data.cpc.globalprecip.html>.

Code availability All analysis code is available upon request from the corresponding author (renxuej@nju.edu.cn) or the first author (dg20280016@mail.nju.edu.cn).

Declarations

Conflict of interest All authors declare that there are no conflicts of interest.

Open Access This article is licensed under a Creative Commons Attribution 4.0 International License, which permits use, sharing, adaptation, distribution and reproduction in any medium or format, as long as you give appropriate credit to the original author(s) and the source, provide a link to the Creative Commons licence, and indicate if changes were made. The images or other third party material in this article are included in the article's Creative Commons licence, unless indicated otherwise in a credit line to the material. If material is not included in the article's Creative Commons licence and your intended use is not permitted by statutory regulation or exceeds the permitted use, you will need to obtain permission directly from the copyright holder. To view a copy of this licence, visit <http://creativecommons.org/licenses/by/4.0/>.

References

- Allen RG, Pereira LS, Raes D, Smith M (1998) Crop evapotranspiration-guidelines for computing crop water requirements-FAO Irrigation and drainage paper 56. Fao Rome 300(9):D05109
- Barrett BS, Henderson GR, Werling JS (2015) The influence of the MJO on the intraseasonal variability of Northern Hemisphere spring snow depth. *J Clim* 28(18):7250–7262. <https://doi.org/10.1175/JCLI-D-15-0092.1>
- Buchard V et al (2017) The MERRA-2 aerosol reanalysis, 1980 onward. Part II: evaluation and case studies. *J Clim* 30(17):6851–6872. <https://doi.org/10.1175/JCLI-D-16-0613.1>
- Bueh C, Xie Z (2015) An objective technique for detecting large-scale tilted ridges and troughs and its application to an east Asian cold event. *Mon Weather Rev* 143(12):4765–4783. <https://doi.org/10.1175/MWR-D-14-00238.1>
- Chang C-P, Lu M-M (2012) Intraseasonal predictability of siberian high and east Asian winter monsoon and its interdecadal variability. *J Clim* 25(5):1773–1778. <https://doi.org/10.1175/JCLI-D-11-00500.1>
- Chou C, Lan C-W (2012) Changes in the annual range of precipitation under global warming. *J Clim* 25(1):222–235. <https://doi.org/10.1175/JCLI-D-11-00097.1>
- DeMott CA, Klingaman NP, Tseng WL, Burt MA, Gao Y, Randall DA (2019) The convection connection: how ocean feedbacks affect tropical mean moisture and MJO propagation. *J Geophys Research: Atmos* 124(22):11910–11931. <https://doi.org/10.1002/2013GL058542>
- Ding Y (1990) Build-up, air mass transformation and propagation of siberian high and its relations to cold surge in East Asia. *Meteorol Atmos Phys* 44(1–4):281–292. <https://doi.org/10.1007/BF01026822>
- Ding Y, Krishnamurti TN (1987) Heat budget of the siberian high and the winter monsoon. *Mon Weather Rev* 115(10):2428–2449. [https://doi.org/10.1175/1520-0493\(1987\)115%3C2428:HBOTS%3E2.0.CO;2](https://doi.org/10.1175/1520-0493(1987)115%3C2428:HBOTS%3E2.0.CO;2)
- Fan L, Yang S, Hu J, Li T (2022) Relationship between the intraseasonal oscillation over mid-high-latitude Eurasia and the stratospheric sudden warming event in February 2018. *Remote Sens* 14(8):1873. <https://doi.org/10.3390/rs14081873>
- Gao Q, Wang L, Li Y, Wang Y (2022) Intra-seasonal features of Winter Extreme Cold events in northeast–North China and Synergistic effects of circulation systems in Mid-high Latitude. *Atmosphere* 13(9):1425. <https://doi.org/10.3390/atmos13091425>
- Ge Y, Gong G (2010) Land surface insulation response to snow depth variability. *J Geophys Research: Atmos* 115. <https://doi.org/10.1029/2009JD012798>
- Gong G, Entekhabi D, Cohen J, Robinson D (2004) Sensitivity of atmospheric response to modeled snow anomaly characteristics. *J Geophys Research: Atmos* 109. <https://doi.org/10.1029/2003JD004160>
- Guan W, Wang L (2023) Mechanism of the wintertime subseasonal surface air temperature variability over Eurasia. *Environ Research: Clim* 2(2):025006. <https://doi.org/10.1088/2752-5295/accd0f>
- Guan B, Waliser DE, Molotch NP, Fetzer EJ, Neiman PJ (2012) Does the Madden–Julian oscillation influence wintertime atmospheric rivers and snowpack in the Sierra Nevada? *Mon Weather Rev* 140(2):325–342. <https://doi.org/10.1175/MWR-D-11-00087.1>
- Guan W, Jiang X, Ren X, Chen G, Lin P, Lin H (2020) The leading intraseasonal variability mode of wintertime surface air temperature over the north American sector. *J Clim* 33(21):9287–9306. <https://doi.org/10.1175/JCLI-D-20-0096.1>
- Hall D, Riggs G (2016) MODIS/Terra Snow Cover Daily L3 Global 0.05 Deg CMG, Version 6, NASA National Snow and Ice Data Center Distributed Active Archive Center, Boulder, Colorado, USA, edited
- Hegyi BM, Deng Y (2017) Dynamical and thermodynamical impacts of high-and low-frequency atmospheric eddies on the initial melt of Arctic Sea Ice. *J Clim* 30(3):865–883. <https://doi.org/10.1175/JCLI-D-15-0366.1>
- Hersbach H et al (2020) The ERA5 global reanalysis. *Q J R Meteorol Soc* 146(730):1999–2049. <https://doi.org/10.1002/qj.3803>
- Holton JR (1973) An introduction to dynamic meteorology. *Am J Phys* 41(5):752–754
- Jeong JH, Linderholm HW, Woo SH, Folland C, Kim BM, Kim SJ, Chen D (2013) Impacts of Snow Initialization on Subseasonal forecasts of Surface Air temperature for the cold season. *J Clim* 26(6):1956–1972. <https://doi.org/10.1175/JCLI-D-12-00159.1>
- Jiang X, Li T, Wang B (2004) Structures and mechanisms of the northward propagating boreal summer intraseasonal oscillation. *J Clim* 17(5):1022–1039. [https://doi.org/10.1175/1520-0442\(2004\)017%3C1022:SAMOTN%3E2.0.CO;2](https://doi.org/10.1175/1520-0442(2004)017%3C1022:SAMOTN%3E2.0.CO;2)
- Jiang Y, Cheung H-N, Li Y, Yang S (2023) Intra-seasonal variation of the wintertime Polar/Eurasia pattern. *Clim Dyn* 61(1–2):813–830. <https://doi.org/10.1007/s00382-022-06612-7>
- Jiao Y, Wu R, Song L (2019) Individual and combined impacts of two eurasian wave trains on intraseasonal east Asian winter monsoon variability. *J Geophys Research: Atmos* 124(8):4530–4548. <https://doi.org/10.1029/2018JD029953>
- Johnson NC, Feldstein SB (2010) The continuum of North Pacific sea level pressure patterns: Intraseasonal, interannual, and interdecadal variability. *J Clim* 23(4):851–867. <https://doi.org/10.1175/5/2009JCLI3099.1>
- Kim H-J, Son S-W, Moon W, Kug J-S, Hwang J (2021) Subseasonal relationship between Arctic and eurasian surface air temperature. *Sci Rep* 11(1):4081. <https://doi.org/10.1038/s41598-021-83486-5>
- Kobayashi S et al (2015) The JRA-55 reanalysis: General specifications and basic characteristics. *J Meteorological Soc Japan Ser II* 93(1):5–48. <https://doi.org/10.2151/jmsj.2015-001>
- Komatsu KK, Takaya Y, Toyoda T, Hasumi H (2023) A submonthly scale causal relation between snow cover and surface air temperature over the autumnal eurasian continent. *J Clim* 1–33. <https://doi.org/10.1175/JCLI-D-22-0827.1>
- Lee J-Y, Wang B, Wheeler MC, Fu X, Waliser DE, Kang I-S (2013) Real-time multivariate indices for the boreal summer intraseasonal oscillation over the Asian summer monsoon region. *Clim Dyn* 40:493–509. <https://doi.org/10.1007/s00382-012-1544-4>
- Li W, Guo W, Hsu P-c, Xue Y (2016) Influence of the Madden–Julian oscillation on tibetan Plateau snow cover at the intraseasonal time-scale. *Sci Rep* 6(1):30456. <https://doi.org/10.1038/srep30456>
- Li Q, Yang S, Wu T, Liu X (2017) Subseasonal dynamical prediction of east Asian cold surges. *Weather Forecast* 32(4):1675–1694. <https://doi.org/10.1175/WAF-D-16-0209.1>
- Li W, Guo W, Qiu B, Xue Y, Hsu PC, Wei J (2018) Influence of tibetan Plateau snow cover on east Asian atmospheric circulation at medium-range time scales. *Nat Commun* 9(1). <https://doi.org/10.1038/s41467-018-06762-5>
- Li W, Qiu B, Guo W, Zhu Z, Hsu PC (2019) Intraseasonal variability of tibetan Plateau snow cover. *Int J Climatol* 40(7):3451–3466. <https://doi.org/10.1002/joc.6407>
- Li W, Qiu B, Guo W, Hsu PC (2021) Rapid response of the east Asian trough to tibetan Plateau snow cover. *Int J Climatol* 41(1):251–261. <https://doi.org/10.1002/joc.6618>
- Lim Y-K (2015) The East Atlantic/West Russia (EA/WR) teleconnection in the North Atlantic: climate impact and relation to Rossby wave propagation. *Clim Dyn* 44(11–12):3211–3222. <https://doi.org/10.1007/s00382-014-2381-4>

- Lin H (2015) Subseasonal variability of north American wintertime surface air temperature. *Clim Dyn* 45:1137–1155. <https://doi.org/10.1007/s00382-014-2363-6>
- Lin H (2018) Predicting the dominant patterns of subseasonal variability of wintertime surface air temperature in extratropical Northern Hemisphere. *Geophys Res Lett* 45(9):4381–4389. <https://doi.org/10.1029/2018GL077509>
- Lin H (2020) Subseasonal forecast skill over the northern polar region in boreal winter. *J Clim* 33(5):1935–1951. <https://doi.org/10.1175/JCLI-D-19-0408.1>
- Linkin ME, Nigam S (2008) The North Pacific Oscillation–West Pacific teleconnection pattern: mature-phase structure and winter impacts. *J Clim* 21(9):1979–1997. <https://doi.org/10.1175/2007JCLI2048.1>
- Liu Y, Wang L, Zhou W, Chen W (2014) Three eurasian teleconnection patterns: spatial structures, temporal variability, and associated winter climate anomalies. *Clim Dyn* 42:2817–2839. <https://doi.org/10.1007/s00382-014-2163-z>
- Llovel W, Willis JK, Landerer FW, Fukumori I (2014) Deep-ocean contribution to sea level and energy budget not detectable over the past decade. *Nat Clim Change* 4(11):1031–1035. <https://doi.org/10.1038/nclimate2387>
- Luo Y, Yang X-Q, Sun L, Tao L (2023) What determines the leading mode of Wintertime Northern Hemisphere snow cover interannual variability? *J Clim* 1–36. <https://doi.org/10.1175/JCLI-D-22-0934.1>
- Luojus K et al (2021) GlobSnow v3. 0 Northern Hemisphere snow water equivalent dataset. *Sci Data* 8(1):163. <https://doi.org/10.1038/s41597-021-00939-2>
- Lynch-Stieglitz M (1994) The development and validation of a simple snow model for the GISS GCM. *J Clim* 7(12):1842–1855. [https://doi.org/10.1175/1520-0442\(1994\)007%3C1842:TDAVOA%3E2.0.CO;2](https://doi.org/10.1175/1520-0442(1994)007%3C1842:TDAVOA%3E2.0.CO;2)
- Ma S, Zhu C (2023) Subseasonal swing of cold and warm extremes between Eurasia and North America in winter of 2020/21: initiation and physical process. *Environ Res Lett* 18(1):014023. <https://doi.org/10.1088/1748-9326/acaabf>
- Madden RA, Julian PR (1971) Detection of a 40–50 day oscillation in the zonal wind in the tropical Pacific. *J Atmos Sci* 28(5):702–708. [https://doi.org/10.1175/1520-0469\(1971\)028%3C0702:DOADOI%3E2.0.CO;2](https://doi.org/10.1175/1520-0469(1971)028%3C0702:DOADOI%3E2.0.CO;2)
- Muñoz-Sabater J et al (2021) ERA5-Land: a state-of-the-art global reanalysis dataset for land applications. *Earth Syst Sci data* 13(9):4349–4383. <https://doi.org/10.5194/essd-13-4349-2021>
- Peng D, Zhou T, Zhang L, Wu B (2018) Human contribution to the increasing summer precipitation in Central Asia from 1961 to 2013. *J Clim* 31(19):8005–8021. <https://doi.org/10.1175/JCLI-D-17-0843.1>
- Qian Y, Hsu PC, Yuan J, Zhu Z, Wang H, Duan M (2022) Effects of subseasonal variation in the East Asian monsoon system on the summertime heat wave in western North America in 2021. *Geophysical Research Letters* 49(8): e2021GL097659
- Qin M, Li S, Xue Y, Han Z (2022) Intraseasonal variability modes of winter surface air temperature over central Asia and their modulation by Greenland Sea ice and central Pacific El Niño–Southern Oscillation. *Int J Climatol* 42(15):8040–8055. <https://doi.org/10.1002/joc.7691>
- Simonnet E, Plaut G (2001) Space-time analysis of geopotential height and SLP, intraseasonal oscillations, weather regimes, and local climates over the North Atlantic and Europe. *Climate Res* 17(3):325–342. <https://doi.org/10.3354/cr017325>
- Song L, Wu R (2019) Intraseasonal snow cover variations over western Siberia and associated atmospheric processes. *J Geophys Research: Atmos* 124(16):8994–9010. <https://doi.org/10.1029/2019JD030479>
- Song L, Wu R, An L (2019a) Different sources of 10-to 30-day intra-seasonal variations of autumn snow over western and eastern Tibetan Plateau. *Geophys Res Lett* 46(15):9118–9125. <https://doi.org/10.1029/2019GL083852>
- Song L, Wu R, Zhu J (2019b) Processes of intraseasonal snow cover variations over the eastern China during boreal winter. *Atmospheric Sci Lett* 20(5):e901. <https://doi.org/10.1002/asl.901>
- Sperber KR (2003) Propagation and the vertical structure of the Madden–Julian oscillation. *Mon Weather Rev* 131(12):3018–3037. [https://doi.org/10.1175/1520-0493\(2003\)131%3C3018:PATVSO%3E2.0.CO;2](https://doi.org/10.1175/1520-0493(2003)131%3C3018:PATVSO%3E2.0.CO;2)
- Stieglitz M, Ducharne A, Koster R, Suarez M (2001) The impact of detailed snow physics on the simulation of snow cover and subsurface thermodynamics at continental scales. *J Hydrometeorol* 2(3):228–242. [https://doi.org/10.1175/1525-7541\(2001\)002%3C0228:TIODSP%3E2.0.CO;2](https://doi.org/10.1175/1525-7541(2001)002%3C0228:TIODSP%3E2.0.CO;2)
- Takaya K, Nakamura H (2005a) Mechanisms of intraseasonal amplification of the cold siberian high. *J Atmos Sci* 62(12):4423–4440. <https://doi.org/10.1175/JAS3629.1>
- Takaya K, Nakamura H (2005b) Geographical dependence of upper-level blocking formation associated with intraseasonal amplification of the siberian high. *J Atmos Sci* 62(12):4441–4449. <https://doi.org/10.1175/JAS3628.1>
- Trenberth KE, Paolino DA (1981) Characteristic patterns of variability of sea level pressure in the Northern Hemisphere. *Mon Weather Rev* 109(6):1169–1189. [https://doi.org/10.1175/1520-0493\(1981\)109%3C1169:CPOVOS%3E2.0.CO;2](https://doi.org/10.1175/1520-0493(1981)109%3C1169:CPOVOS%3E2.0.CO;2)
- Wang M, Tan B (2020) Two types of the Scandinavian pattern: their formation mechanisms and climate impacts. *J Clim* 33(7):2645–2661. <https://doi.org/10.1175/JCLI-D-19-0447.1>
- Wang S, Ma D, Sobel AH, Tippett MK (2018) Propagation characteristics of BSISO indices. *Geophys Res Lett* 45(18):9934–9943. <https://doi.org/10.1029/2018GL078321>
- Wheeler MC, Hendon HH (2004) An all-season real-time multivariate MJO index: development of an index for monitoring and prediction. *Mon Weather Rev* 132(8):1917–1932. [https://doi.org/10.1175/1520-0493\(2004\)132%3C1917:AARMMI%3E2.0.CO;2](https://doi.org/10.1175/1520-0493(2004)132%3C1917:AARMMI%3E2.0.CO;2)
- Xiang B, Lin SJ, Zhao M, Johnson NC, Yang X, Jiang X (2019) Subseasonal week 3–5 surface air temperature prediction during boreal wintertime in a GFDL model. *Geophys Res Lett* 46(1):416–425. <https://doi.org/10.1029/2018GL081314>
- Xiang B, Sun YQ, Chen JH, Johnson NC, Jiang X (2020) Subseasonal prediction of land cold extremes in boreal wintertime. *J Geophys Research: Atmos* 125(13). <https://doi.org/10.1029/2020JD032670>
- Xie P, Chen M, Yang S, Yatagai A, Hayasaka T, Fukushima Y, Liu C (2007) A gauge-based analysis of daily precipitation over East Asia. *J Hydrometeorol* 8(3):607–626. <https://doi.org/10.1175/JHM583.1>
- Xiu J, Jiang X, Zhang R, Guan W, Chen G (2022) An intraseasonal mode linking wintertime surface air temperature over Arctic and Eurasian continent. *J Clim* 35(9):2675–2696. <https://doi.org/10.1175/JCLI-D-21-0495.1>
- Xu W, Ma H, Wu D, Yuan W (2017) Assessment of the daily cloud-free MODIS snow-cover product for monitoring the snow-cover phenology over the Qinghai-Tibetan Plateau. *Remote Sens* 9(6):585. <https://doi.org/10.3390/rs9060585>
- Xu X, Li F, He S, Wang H (2018) Subseasonal reversal of east Asian surface temperature variability in winter 2014/15. *Adv Atmos Sci* 35:737–752. <https://doi.org/10.1007/s00376-017-7059-5>
- Yang D, Ingersoll AP (2013) Triggered convection, gravity waves, and the MJO: a shallow-water model. *J Atmos Sci* 70(8):2476–2486. <https://doi.org/10.1175/JAS-D-12-0255.1>

- Yang S, Li T (2016) Intraseasonal variability of air temperature over the mid-high latitude Eurasia in boreal winter. *Clim Dyn* 47:2155–2175. <https://doi.org/10.1007/s00382-015-2956-8>
- Yang S, Zhu Z, Cui J, Yang Y (2019) Regulation of the intraseasonal oscillation over mid-to-high latitude Eurasia on winter surface air temperature over China. *Dynamics of Atmospheres and Oceans* 86: 63–72. <https://doi.org/j.dynatmoce.2019.03.003>
- Yao Y, Lin H, Wu Q (2015) Subseasonal variability of precipitation in China during boreal winter. *J Clim* 28(16):6548–6559. <https://doi.org/10.1175/JCLI-D-15-0033.1>
- Yao S, Sun Q, Huang Q, Chu P (2016) The 10–30-day intraseasonal variation of the east Asian winter monsoon: the temperature mode. *Dyn Atmos Oceans* 75:91–101. <https://doi.org/10.1016/j.dynatmoce.2016.07.001>
- You Q et al (2020) Review of snow cover variation over the Tibetan Plateau and its influence on the broad climate system. *Earth Sci Rev* 201:103043. <https://doi.org/10.1016/j.earscirev.2019.103043>
- Zhang T (2005) Influence of the seasonal snow cover on the ground thermal regime: an overview. *Rev Geophys* 43(4). <https://doi.org/10.1029/2004RG000157>
- Zhang D, Shi N, Tajie S (2022) Mechanisms of the subseasonal influences of scandinavian events on winter surface air temperature over Eastern China. *Atmos Res* 268:105994. <https://doi.org/10.1016/j.atmosres.2021.105994>
- Zhong W, Wu Z (2022) Subseasonal variations of eurasian wintertime surface air temperature: two distinct leading modes. *Clim Dyn* 59(1–2):85–108. <https://doi.org/10.1007/s00382-021-06118-8>
- Zhou F, Shi J, Liu M-H, Ren H-C (2023) Linkage between the NAO and siberian high events on the intraseasonal timescale. *Atmos Res* 281:106478. <https://doi.org/10.1016/j.atmosres.2022.106478>
- Zhu T, Yang J (2021) Two types of mid-high-latitude low-frequency intraseasonal oscillations near the Ural Mountains during boreal summer. *J Clim* 34(11):4279–4296. <https://doi.org/10.1175/JCLI-D-20-0589.1>
- Zhu T, Yang J, Wang B, Bao Q (2023) Boreal summer extratropical intraseasonal waves over the eurasian continent and real-time monitoring metrics. *J Clim* 36(12):3971–3991. <https://doi.org/10.1175/JCLI-D-22-0788.1>

Publisher's Note Springer Nature remains neutral with regard to jurisdictional claims in published maps and institutional affiliations.